INVESTIGATIONS OF SCALAR TRANSFER COEFFICIENTS IN FOG DURING THE COUPLED BOUNDARY LAYERS AND AIR-SEA TRANSFER EXPERIMENT: A CASE STUDY

by

Robert Farrington Crofoot

B.S., The Citadel, The Military College of South Carolina (1996)

Submitted in partial fulfillment of the requirements for the degree of

MASTER OF SCIENCE
at the
MASSACHUSETTS INSTITUTE OF TECHNOLOGY
and the
WOODS HOLE OCEANOGRAPHIC INSTITUTION

September 2004

Author...
Joint Program in Applied Ocean Physics and Engineering
Massachusetts Institute of Technology and Woods Hole Oceanographic Institution

Certified by...
James B. Edson
Senior Scientist, Woods Hole Oceanographic Institution
Thesis Supervisor

Certified by...
Robert A. Weller
Senior Scientist, Woods Hole Oceanographic Institution
Thesis Reader

Approved by...
Mark A. Grosenbaugh
Chairman, Joint Committee for Applied Ocean Science and Engineering
Massachusetts Institute of Technology and Woods Hole Oceanographic Institution
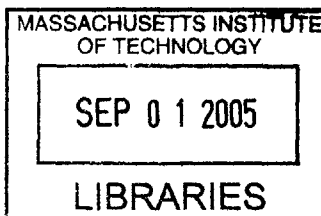
INVESTIGATIONS OF SCALAR TRANSFER COEFFICIENTS IN FOG DURING
THE COUPLED BOUNDARY LAYERS AND AIR-SEA TRANSFER EXPERIMENT:
A CASE STUDY
by
Robert Farrington Crofoot

Submitted in partial fulfillment
of the requirements for the degree of
Master of Science
at the
MASSACHUSETTS INSTITUTE OF TECHNOLOGY
and the
WOODS HOLE OCEANOGRAPHIC INSTITUTION
September 2004

ABSTRACT

The uncertainty in the determination of the momentum and scalar fluxes remains one of the main obstacles to accurate numerical forecasts in low to moderate wind conditions. For example, latent heat fluxes computed from data using direct covariance and bulk aerodynamic methods show that there is good agreement in unstable conditions when the latent heat flux values are generally positive. However, the agreement is relatively poor in stable conditions, particularly when the moisture flux is directed downward. If the direct covariance measurements are indeed accurate, then they clearly indicate that the bulk aerodynamic formula overestimate the downward moisture flux in stable conditions. As a result, comparisons of the Dalton number for unstable and stable conditions indicate a marked difference in value between the two stability regimes.

Investigations done for this thesis used data taken primarily at the Air-Sea Interaction Tower (ASIT) during the Coupled Boundary Layers and Air-Sea Transfer (CBLAST) Experiment 2003 from the 20-27 August 2003. Other data from the shore based Martha's Vineyard Coastal Observatory (MVCO) and moored buoys in the vicinity of the ASIT were also incorporated. During this eight day period, the boundary layer was often characterized by light winds, a stably stratified surface layer and a swell dominated wave field. Additionally, the advection of warm moist air over cooler water resulted in fog formation and a downward flux of moisture on at least three occasions. Therefore, a primary objective of this thesis is to present a case study to investigate the cause of this shortcoming in the bulk formula under these conditions by examining the physical processes that are unique to these boundary layers. Particular attention will be paid to the behavior of the Dalton number in a stable marine atmospheric boundary layer under foggy conditions using insights derived from the study of fog formation and current flux parameterization methods.

Thesis Supervisor: Dr. James B. Edson
Title: Senior Scientist

ACKNOWLEDGEMENTS

TABLE OF CONTENTS

LIST OF FIGURES

Figure

Page

LIST OF TABLES

8

1. INTRODUCTION

1.1 Background

Over the past several years, WHOI researchers and their colleagues have made significant progress in obtaining measurements of turbulent fluxes in the marine atmospheric boundary layer (MABL) through recent field experiments such as TOGA COARE (Fairall, Bradley et al. 1996), RASEX (Mahrt, Vickers et al. 1996), MBL (Grachev, Fairall et al. 2003), COOP (Hara, Bock et al. 1998), and FASTEX (Hare, Persson et al. 1999). The majority of these measurements were collected in near-neutral to slightly unstable conditions. The culmination of these efforts resulted in the state of the art TOGA COARE 3.0 (TC 3.0) bulk aerodynamic (BA) parameterizations (Fairall, Bradley et al. 2003). This BA parameterization has been widely accepted and proven as the field standard for turbulent flux measurements in the MABL, particularly for unstable conditions. The current parameterization for stable conditions is based on the SHEBA (Persson, Fairall et al. 2002) experiment which was conducted over ice. However, several of the aforementioned experiments collected data in stable conditions when the direct covariance (DC) and TC 3.0 latent heat flux (LHF) differ significantly. Specifically, this data indicated that when stable conditions existed, particularly in fog, a downward (negative) flux of moisture to the sea surface was frequently observed. A negative surface flux means that the ocean is gaining heat and the atmosphere is losing heat. As can be seen in figure 1.1, TC 3.0 tends to overestimate the LHF when compared to DC measurements in these conditions. Additionally, with the exception of RASEX and MBL, these experiments did not measure flux profiles and neither RASEX nor MBL was set up to examine mean and flux profile relations for scalars such as moisture and heat. As a result, we still rely heavily on overland measurements such as those made during the Kansas (Izumi 1971) and Minnesota (Champagne, Friehe et al. 1977) field campaigns for flux profile relationships, in addition to the above mentioned relationships over ice, for unstable and stable MABLs.

Recently, flux profile relationships in the MABL were measured during the GasEx and FAIRS experiments (Edson, Zappa et al. 2004; Hintsa, Dacey et al. 2004).

The data from these experiments exhibited good agreement with overland experiments for unstable conditions, but were unable to evaluate results in stable conditions due to a lack of sufficient data. In addition, other complications arose that are inherent to any experiment where measurements are taken strictly from ship or buoy-based instrumentation platforms. These issues arise from the requirement that corrections must be made to remove the effects of platform motion, localized

Figure 1.1 CBLAST Latent Heat Fluxes August 20-27, 2003
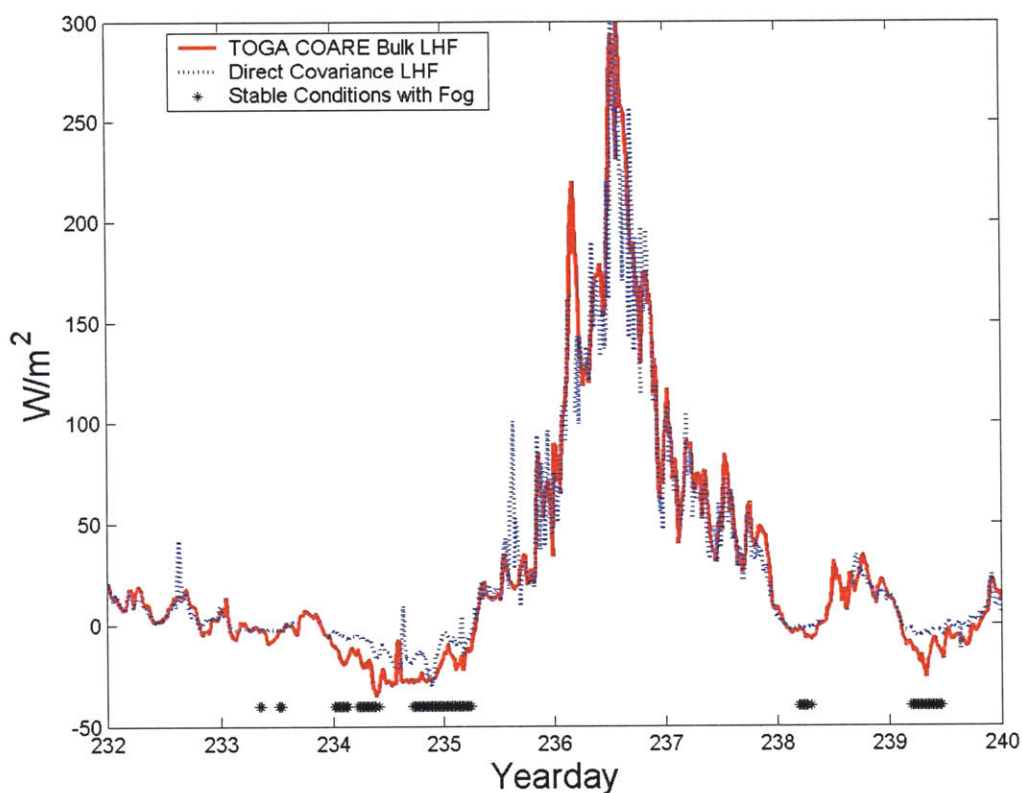
heating, flow distortion (particularly the ship-based GasEx measurements) and instrument contamination due to the adverse effects of the marine environment such as sea spray, corrosion and wave action.

The Office of Naval Research (ONR) funded the Coupled Boundary Layers and Air-Sea Transfer Low Wind (CBLAST-Low) experiment to further the progress already

achieved in the previous field experiments under light to moderate wind conditions. The experiment was designed to measure fluxes and their associated profiles so that every term within the turbulent kinetic energy and scalar variance (SV) budgets were calculated as described in section 2.3. An optimal suite of instrumentation deployed from aircraft, ships, buoys, and fixed-towers acquired the most complete and comprehensive data set ever collected in the MABL. Simultaneous meteorological and oceanographic measurements provided scientists with a unique opportunity to fully investigate the complex physical processes which drive the energy exchange between the ocean and atmosphere.

One of the primary objectives of the knowledge gained from the CBLAST experiment is to aide in the development of improved parameterizations for possible use in the Navy's mesoscale model, the Coupled Ocean-Atmosphere Mesoscale Prediction System (COAMPS). Despite its name, COAMPS is not, as of yet, truly coupled. This is mostly attributable to the challenges alluded to previously. In particular, as with most models, accurate boundary conditions are essential to proper initialization and subsequent proper operation of the model. The complexities of the marine environment make this a formidable task and are introduced in further detail here.

1.2 Challenges

The differences between the land and marine environments are quite distinct. The large heat capacity of the ocean, the relative importance of advective processes, and the complexity of the air-sea interface make accurate forecasts of sea surface temperature (SST) challenging. The presence of waves introduces complications that invalidate the application of parameterizations derived over land to grid points near the surface. For example, modification of the near surface turbulence by the waves impacts the fluxes driven by the turbulence. This invalidates one of the primary assumptions of commonly applied scaling laws used in the parameterization of these fluxes known as Monin-Obukhov similarity described in section 3.1. In addition, the effect of fog in a stable

11

boundary layer on the turbulent flux profiles over the ocean is, at present, relatively unknown. With these complications and despite the progress made in recent years, the operation of truly coupled mesoscale prediction models remains a challenge.

1.2.1 Sea Surface Temperature

In the case of COAMPS and other models used over the ocean, an accurate prediction of the evolution of SST is a paramount factor. Accurate sea surface temperatures are required to yield accurate heat flux estimations from bulk parameterizations. Likewise, accurate flux estimates are necessary to provide realistic sea surface temperatures and to keep the predictions from "running away", particularly in regions or times when data assimilation is an issue. This proves quite difficult as SST may have rich time and space variability in low winds with large spatial gradients from onshore to offshore. Additionally, the oceanic boundary layer (OBL) changes in thickness and temperature from onshore to offshore, depending on, e.g., whether upwelling or downwelling favorable winds are present and whether the OBL is influenced by the bottom boundary layer (Weller 2004). Due to the huge heat capacity of the ocean as compared to the atmosphere, latent and sensible heat fluxes are strongly correlated with the slowly evolving SST field (Farrar 2004). If there is a positive LHF, the effect of evaporation of the sea surface creates a cool skin effect. If the LHF is negative, the effect of condensation on the sea surface creates a warm skin effect. Either process produces a temperature gradient in the uppermost millimeter of the sea surface of a few tenths of a degree Kelvin. Bulk measurements of sea temperature cannot account for this effect so other methods must be employed such as infrared radiometry. However, if fog is present, these may give inaccurate measurements.

SST can also be affected by surface films or surfactants composed primarily of phytoplankton. Bands of these surfactant slicks are related to SST anomolies. These slicks reduce the surface tension of the sea surface thereby modulating physical transfer

processes. These slicks erode with increasing winds and so tend to be more prevalent in low wind conditions such as those experienced during CBLAST (Frew 2004).

1.2.2 Wave Effects

Waves have a direct effect on the momentum and turbulent kinetic energy (TKE) fluxes. The physical argument is that momentum can be carried by both tangential stress (i.e. shear stress) and normal stress (i.e. form drag) created by the interaction between the pressure and wave fields, which causes interaction between the pressure and velocity field away from the surface. The interaction drives fluxes and flux divergences that appear as source/sink terms in the TKE and momentum budgets (Janssen 1999). However, the equivalent of a normal stress does not exist in the heat and moisture budget equations due to the absence of pressure terms. This translates to the absence of a wave induced heat or moisture flux over waves (Edson, Zappa et al. 2002; Stull 1988). Instead, the effect of waves on heat and moisture fluxes is an indirect result of the waves modifying the turbulence responsible for transporting these passive scalars. As a result, it is assumed that the scalar fluxes are less affected by waves.

The form drag of the longer, fastest moving waves can actually impart momentum back into the atmosphere (Grachev, Fairall et al. 2003). This effect of form drag on momentum exchange and the near surface velocity profile is a function of wave age and stability. In light winds, old seas, and stable conditions, the wave generated winds can produce a low level jet at 50-100 meters in the MABL (Sullivan 2004). Therefore, surface wave effects are essential for coupling the MABL to the OBL in any model (Edson 2004; Hristov 2004; McWilliams 2004; Sullivan 2004; Vickers 2004). This region where the wave effects have the most pronounced affect on the atmosphere is called the wave boundary layer (WBL). At present, the WBL is, in quantitative terms, poorly understood. As a result, no generally accepted definition of the height of the WBL exists. Some modelers assume that it is limited to the region $\frac{z}{\sigma_H} \ll 1$, where σ_H is the significant wave height of the dominant waves and z is some reference height. Some

recent field campaigns have shown that some terms like the pressure transport term in the TKE budget equation are influenced by waves up to heights where $k_p z \approx 2$ where k_p is the peak wave number of the dominant waves, suggesting a much thicker WBL (Edson, Zappa et al. 2002). Further knowledge on the WBL gained through the CBLAST data set should provide valuable insight into the details of the physics related to this region.

1.2.3 The Stable Boundary Layer

In the unstable MABL, current parameterization methods perform relatively well except for very near the surface in the WBL. Like its ocean counterpart, the greatest challenge in micrometeorology is to improve our understanding of the stable MABL, which is often characterized by light winds and fog. Shallow stable boundary layers are common in coastal regions and are often characterized by a turbulent flow that is very weak or collapsed entirely (Sullivan 2004; Vickers 2004; Mahrt 2004). In fact, the boundary layer is often indefinable in very stable conditions. Additionally, the low winds mean that there will be less wind generated waves, which allows swell to dominate the wave field. This was a common feature during CBLAST. As previously mentioned, these swell waves, if they are moving fast enough, can impart positive momentum flux to the boundary layer (Grachev, Fairall et al. 2003).

1.2.4 Fog

The requirement to accurately predict fog and low-level clouds are big problems for all mesoscale models (Wang 2004). The formation process of fog is different from that of a cloud. In cloud formation, the air is saturated by adiabatic cooling due to a falling pressure in rising air parcels. Fog occurs in the lower atmosphere within a few meters, few tens of meters, or at most hundreds of meters of the surface, and is commonly driven by horizontal advection and vertical mixing of temperature and water vapor (Binhua 1985). This is especially true in the marine environment where advective

14

processes play a key role. However, whether or not the exchange of heat and mass leads to fog formation depends on the synoptic state of the atmosphere and the underlying SST. Clearly, air-sea interaction plays a key role in fog formation over the ocean. As a result, fog presents a multitude of difficulties to scientists and modelers due to the complex thermodynamic processes that lend to its formation.

How fog affects the momentum, heat and moisture flux profiles is largely unknown as few if any field experiments have emphasized turbulence measurements in fog (Welch and Wielicki 1986). What observations have shown (mostly over land) is that fogs are not uniform, but have high frequency variations in most measured variables. They also have quasi-periodic oscillations in measured properties such as temperature, liquid water, visibility, wind speed, radiation, and turbulence generation. Periods of oscillation range from 5-30 minutes depending upon the cause of the oscillations. Some attribute the quasi-periodic oscillations to gravity waves propagating at the top of the boundary layer. Longer period oscillations may be caused by a fluctuating balance between radiational cooling at the fog top and turbulence generation. Shorter period oscillations may be caused by advection of fog cells past the observation site. If wind direction and wind speed vary slowly with height, then two dimensional cells are typically formed with longitudinal bands elongated along the wind direction (Welch and Wielicki 1986).

There are three primary processes which influence fog formation: cooling, moistening, and the vertical mixing of air parcels with different humidities and temperatures. In the marine environment, warm, moist air moving over cooler water results in sea fog, (sometimes called advection fog), while cool, dry air moving over warmer water generates steam fog (sometimes called radiation fog). Historically fog has been classified by these two main categories: radiation and advection (Lundquist 2000). The dominant fog species present during the case study period was advection fog. Therefore the remainder of this discussion will focus only on advection fog caused by the advection of warm, moist air over the relatively cool water south of Martha's Vineyard.

One school of thought is that the cool water in contact with the air causes the air to cool to its dew point and condense, forming fog. However, this layer of air by contact is generally very thin, and condensation, if any, is thought to occur in a very thin layer, so that the fog formed may also be shallow (Binhua 1985). However, advection fog often exists in thick layers. Therefore, another school of thought suggests that the formation of fog next to a cold surface is not a direct consequence of the cooling, but rather an effect of turbulent mixing of nearly saturated eddies at different temperatures. If a warm air parcel advectively flows over a cold surface and does not drive away the cold air originally on underlying the surface, but horizontally mixes with the cold air, the advection cooling is accomplished by the mixing of warm and cold air. When cold and warm air parcels advectively flow into each other, the warm air often vertically mixes with the cold air below, and heat (also water vapor) is transported downward due to turbulent exchange.   Still another hypothesis, based on modeling and measurements of fog, states that a virtual cessation of turbulent mixing is necessary before fog can form and persist by the radiational cooling of droplets, i.e., turbulent mixing may inhibit fog formation at the surface, especially in light winds (Gerber 1981; Turton and Brown 1987). While other observations have suggested that cessation of turbulent mixing may not be required; it is generally accepted that once fog forms, radiational cooling of the droplets causes a development and thickening of the fog and that turbulence and radiational cooling interact in controlling fog. For example, Turton and Brown (1987) suggest that the development of mature fog is dominated by radiative cooling from the fog top. Clearly, however, there is still considerable uncertainty as to the processes responsible for fog formation (Welch, Ravichandran et al. 1986).

Advection fog is very dense fog that typically only dissipates when the wind direction shifts, or when the fog is advected over warmer land. Over the ocean, dissipation occurs when the wind advects the fog across the horizontal SST gradients. When warmer water is reached, the increased buoyancy flux often pushes air parcels up through the inversion. This causes the entrainment of drier air from aloft to break up the fog layer, causing the fog to lift, form stratus, and eventually disappear.

Light wind speeds are considered necessary for fog formation and, in fact, fog is most often associated with lower wind speed events over land. However, higher wind speeds can coexist within advection fog because the relatively smooth sea surface generates less friction, resulting in less shear generated turbulence. This type of fog often occurs at latitude of about 42° N in the vicinity of the northern wall of the Gulf Stream. Once the fog forms over the continental shelf, radiation is much less important in controlling this fog than SST gradients. In coastal waters, sea currents act on the transportation of waters with different temperatures, thus determining the distribution and variation of the temperatures and their gradients. So, they provide the necessary conditions for the formation, continuation and dissipation of advection fogs. Therefore the primary hydrological element directly related to advection fog should be the sea water temperature, especially the SST and its gradient (Binhua 1985; Lundquist 2000).

The challenges presented by fog to modelers are clearly evident. In summary, the strong atmospheric stability associated with fog typically has lighter winds, shorter periods of oscillation, and greater likelihood of patchy fog. Dense fog is composed of highly structured and sharply defined local regions (Welch and Wielicki 1986). The constant flux layer may only be a few meters deep in fogs, with patchy regions of turbulence above this layer. Due to the scarcity of turbulence measurements in fogs, there is great uncertainty as to the proper parameterization of various coefficients required in the higher-order closure formulations (Welch, Ravichandran et al. 1986). In addition, boundary layer models usually place the first grid point in air several meters above the surface. However, it is believed that important processes in fog formation take place below one meter and it is necessary to model them explicitly. Additionally, most models are currently unable to accurately reproduce the light winds observed near the surface which are essential for fog formation and continuation. This defect is a common characteristic of boundary layer models when applied to stable conditions and is believed to be due to the finite size of the roughness elements (Turton and Brown 1987).

1.2.5 COAMPS

Models such as COAMPS that rely on flux parameterizations based on MABL experiments conducted primarily in unstable conditions (Fairall, Bradley et al. 2003) have difficulties predicting fog in stable conditions in the marine environment. As a result, the parameterizations for stable boundary layers, particularly when fog is present, are very questionable. The inadequate vertical and horizontal resolution is another issue which makes model forecasting difficult. For fluxes, COAMPS uses the MOS based parameterization from Louis (1979), which is a traditional one and a half-order turbulence closure model. This model predicts turbulent kinetic energy and determines a mixing length to derive a turbulent exchange coefficient which will be discussed in chapter 3. According to one of the COAMPS modelers (Wang 2004), this parameterization gives virtually the same results as TC 3.0 over the ocean in stable conditions. At present, COAMPS has no particular scheme to forecast fog, although the phase change effect in turbulence is included in the TKE equation. Grid-scale liquid water (mass and droplet number) is predicted using a two-moment scheme, and fog formation occurs when super saturation exists at the first level (10 meters). This is common for boundary layer models to place the first grid point several meters above the surface. However, as previously mentioned, the disadvantage is that the important processes in fog formation take place below one meter (Wang 2004; Binhua 1985; Turton and Brown 1987).

The coupling of COAMPS is still a work in progress. Presently, the boundary conditions for COAMPS are provided by another model, Navy Operational Global Atmospheric Prediction System (NOGAPS), which initializes COAMPS at 0000Z and 1200Z. SST is provided by satellite derived estimates and then COAMPS makes its own SST analysis at the surface every time it runs using optimum interpolation techniques. With respect to performance, COAMPS has a tendency to overestimate air temperature, potential temperature, latent and specific heat fluxes in amplitude, but captures variability reasonably well. It underestimates longwave radiation, which compensates for the

overestimation of the heat fluxes in the heat budget. This thesis will attempt to aid in the identification of some of the physical processes that complicate forecasting for mesoscale prediction models such as COAMPS in its current state and provide further insight towards the development of improved parameterizations for these processes and the ultimate coupling of COAMPS to an oceanic prediction model.

2. EXPERIMENT

2.1 Data Collection Site

The experiment was conducted predominantly in coastal waters south of Martha's Vineyard (figure 2.1) with an additional component located on Nantucket Island.

Figure 2.1 CBLAST Data Collection Site
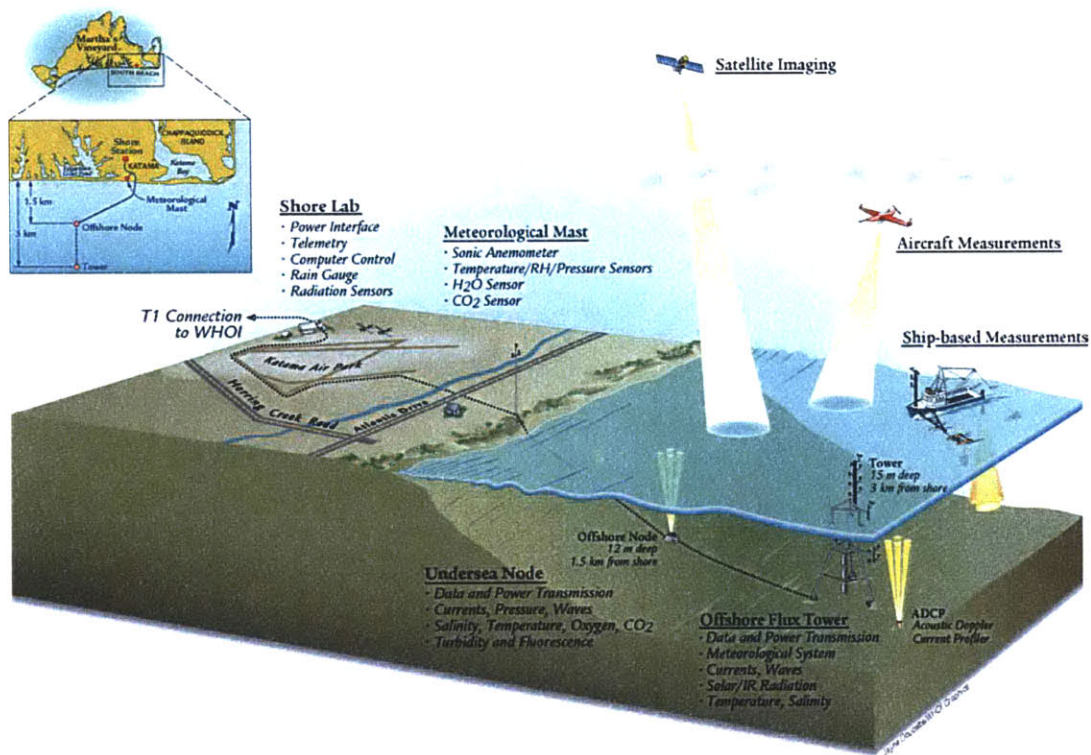
The approximately 25 kilometer long southern shoreline of Martha's Vineyard is nearly straight with homogenous alongshore topography to the west of Wasque Shoals. The shoreline faces the predominant southwesterly winds and seas from the open ocean. Therefore, it is an ideal site for investigating MABL physical processes with minimal land based influences during extensive periods of onshore winds (Austin, Edson et al.

2002). Instrumentation assets deployed during CBLAST included the MVCO, Nantucket Island site, two aircraft, the vessel Nobska, the fixed offshore ASIT, five heavy moorings (three with full meteorological packages), nine of ten light moorings (one was lost), and seafloor based instrumentation.

The combination of all of these assets provided a time series from seven spatially separated locations with meteorological data and eighteen locations with oceanographic data. Figure 2.2 illustrates some of the instrument locations in the CBLAST data collection region:

Figure 2.2 CBLAST Offshore Array
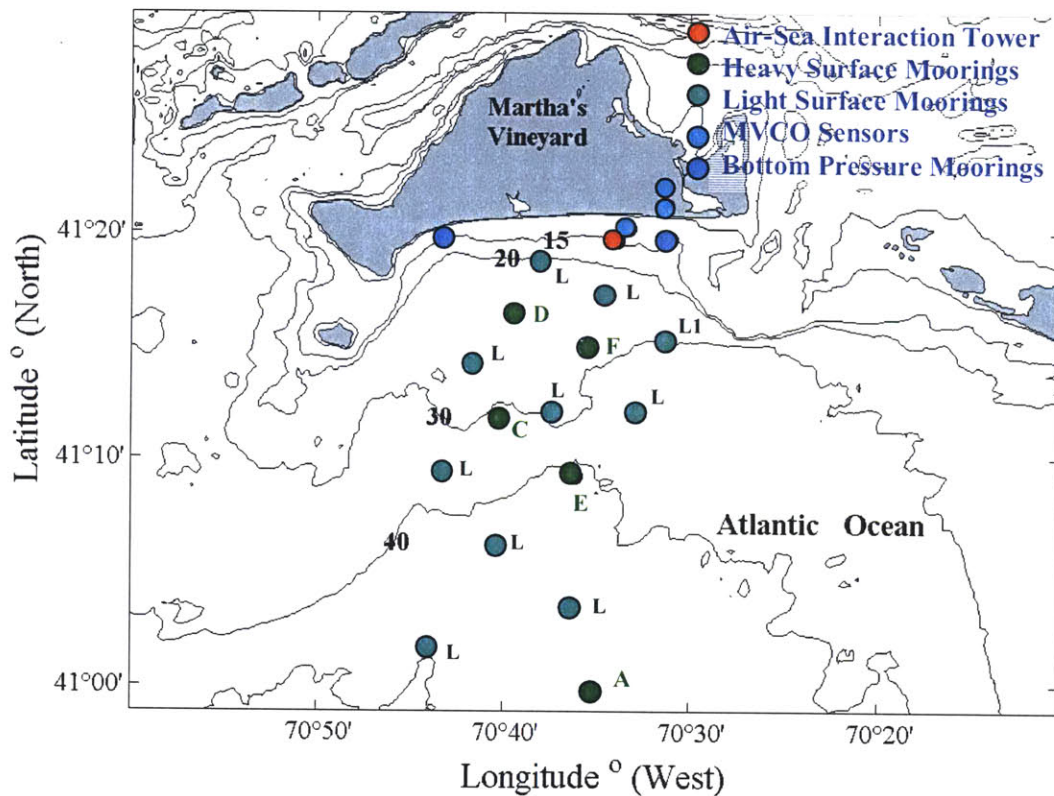
The point measurements are being combined with the spatial surveys from the two aircraft and the Nobska to investigate the processes that exchange momentum, heat, and mass across and within the coupled boundary layer (CBL) (Edson, McGillis et al. 2003).

2.2 Martha's Vineyard Coastal Observatory

The MVCO includes a small shore lab located 1.5 kilometers inland and a 10 meter meteorological mast located 50 meters inshore of the shoreline and just behind the present location of the dunes. The mast rises approximately 8 meters above the dunes and 13 meters above mean sea level. There is also a subsurface node mounted on the seafloor in 12 meters water depth, 1.5 kilometers offshore. The node refers to electrical components that power the instruments and telemeter the data to shore. The data from the meteorological mast, undersea node and associated instrumentation are connected directly to the shore lab via an embedded electro-optic power cable. The shore lab is connected to WHOI via a T-1 data line.

The site for the meteorological mast is particularly attractive because the gently sloping topography at the beach allows sensor deployment above the internal boundary layer and most of the flow distortion induced by the shoreline transition from ocean to beach and dunes. This places the fast response instruments in marine air for onshore winds. The sensors include a 3 axis ultrasonic anemometer which also provides fast response temperature measurements derived from its sound speed measurements and an IR hygrometer/ CO_2 sensor. Additional sensors measure the mean wind speed and direction, relative humidity, temperature, and pressure. The mast also supports a camera to visually monitor the cloud coverage and surface wave conditions in its field of view. A 10 meter mast extending above the laboratory holds sensors to measure solar and infrared radiation, rainfall rate, temperature, humidity, wind speed, and direction. The first phase of the MVCO which included the lab, meteorological mast, and offshore node, became operational by June 2001 (Edson and McGillis 2003; Austin, Edson et al. 2002).

2.3 Air-Sea Interaction Tower

The ASIT is located 3 kilometers due south of Edgartown Great Pond (see figures 2.1 and 2.2) and spans the water column at a depth of 15 meters and to a height above the sea surface of 22 meters (figure 2.3). The tower is connected directly to shore using fiber optic cable. The ASIT was completed late in the summer of 2002 and was outfitted with an electronics node and directly connected to MVCO in the fall of 2002 to provide data transmission and power directly from shore. The ASIT was instrumented starting in the spring of 2003 in preparation of the IOP.

Figure 2.3 Air-Sea Interaction Tower
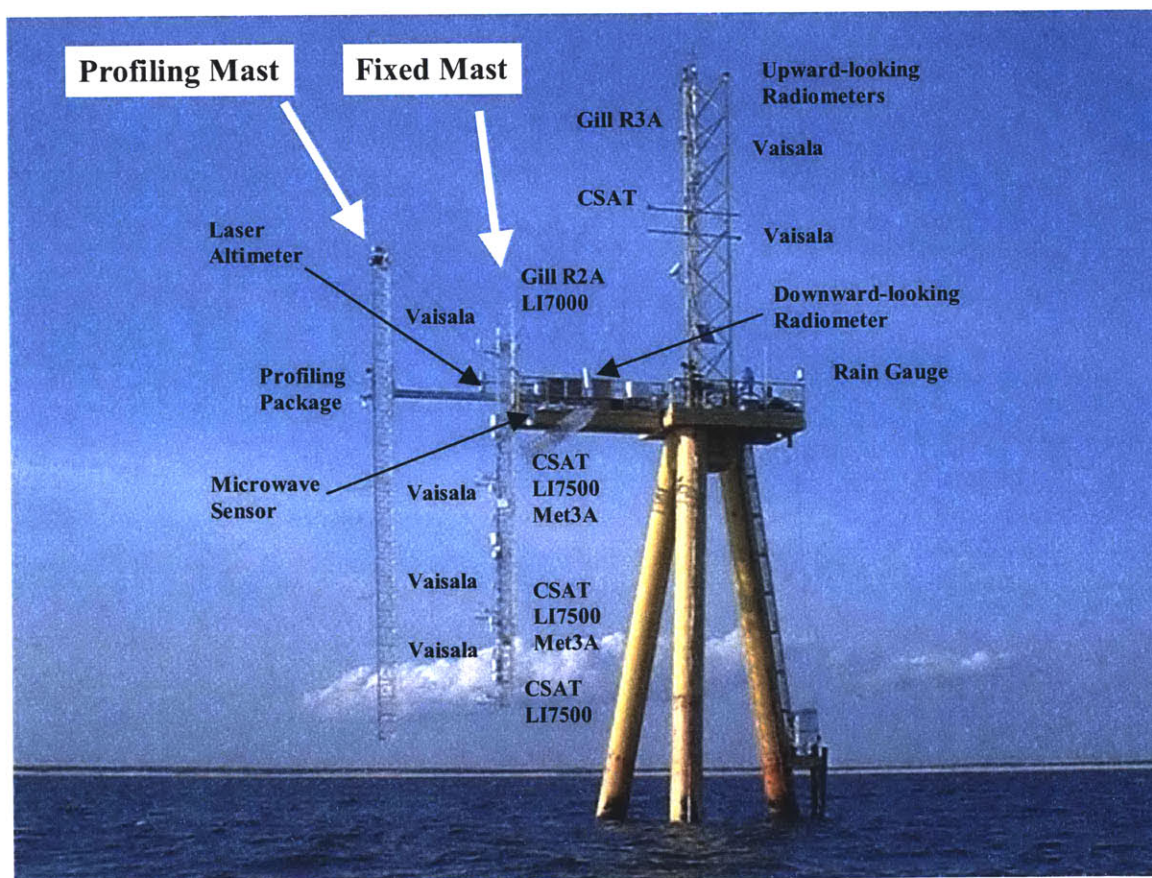
The 22 meter section of the tower in the MABL was equipped with a fixed mast that held fast response sonic anemometer/thermometers paired with IR hygrometers at the lowest three levels. The combination of the sonic anemometer, sonic thermometer and infrared hygrometer provide DC estimates of the momentum, TKE, SV, sensible heat, and latent heat fluxes.

In addition, sensors were deployed which are capable of measuring static pressure fluctuations at two of those levels to estimate the pressure flux. The dissipation rates of TKE and SV were computed from these sensors using inertial sub range estimates. Fixed sensors capable of measuring the mean profiles were deployed within the vertical array. Additionally, a profiling mast was deployed toward the end of the IOP to measure mean profiles to go with the turbulent fluxes through mid-October. A distinct advantage of this arrangement is that it provides the ability to measure all the terms of the one dimensional TKE and SV budgets:

$$-\overline{u'w'}\frac{\partial U}{\partial z} - \overline{v'w'}\frac{\partial V}{\partial z} + \frac{g}{\Theta_v}\overline{w'\theta_v'} - \frac{1}{\rho_a}\frac{\partial \overline{w'p'}}{\partial z} - \frac{\partial \overline{w'e'}}{\partial z} = \varepsilon \qquad (2.3.1)$$

$$\overline{w'\theta'}\frac{\partial \Theta}{\partial z} - \frac{1}{2}\frac{\partial \overline{w'\theta'^2}}{\partial z} = N_\theta \qquad (2.3.2)$$

$$\overline{w'q'}\frac{\partial Q}{\partial z} - \frac{1}{2}\frac{\partial \overline{w'q'^2}}{\partial z} = N_q \qquad (2.3.3)$$

where $e = 0.5(u^2 + v^2 + w^2)$ is the TKE; u', v', and w' are the three velocity component

fluctuations; $\overline{u'w'}, \overline{v'w'}, \overline{w'\theta'}, \overline{w'q'}, \overline{w'p'}, \overline{w'e'}, \overline{w'\theta'^2}$ and $\overline{w'q'^2}$ are the kinematic forms of the

along wind momentum, crosswind momentum, sensible heat, latent heat, pressure, TKE fluxes, temperature variance, and humidity variance respectively; ρ_a is the density of dry air; ε, N_θ, and N_q are the TKE, temperature variance, and humidity variance dissipation

respectively; and $\frac{\partial U}{\partial z}, \frac{\partial V}{\partial z}, \frac{\partial \theta}{\partial z}$, and $\frac{\partial Q}{\partial z}$ are the mean vertical gradients of velocity,

potential temperature, and humidity. The first two terms on the left side of (2.3.1) represent the generation of mechanical turbulence through shear, while the third term

represents the production (suppression) of turbulence through convection (stratification). The fourth and fifth terms neither produce nor consume TKE, instead they act to redistribute TKE within the MABL through pressure and energy transport. The first terms on the left side of (2.3.2) and (2.3.3) represent production of SV, the second terms act to redistribute the variance (Edson and Fairall 1998).

The DC fluxes of sensible heat, latent heat, and stress are expressed:

$$Q_h = \rho_a c_{pa} \overline{w'\theta'}$$
$$Q_e = \rho_a L_e \overline{w'q'} \quad\quad (2.3.4)$$
$$\overline{\tau} = \rho_a \left[\hat{i}\,\overline{u'w'} + \hat{j}\,\overline{v'w'} \right]$$

where c_p is the specific heat at constant pressure, L_e is the latent heat of vaporization of water, Q_h is the DC sensible heat flux, Q_e is the DC LHF, and $\overline{\tau}$ is the DC stress vector, and $\overline{w'\theta'}, \overline{w'q'}$, and $\overline{u'w'}$ are the heat, moisture and momentum fluxes respectively (Fairall, Bradley et al. 1996).

The profile measurements from this setup will also be used to provide an in situ calibration of the fixed sensors on the rest of the ASIT. Additional measurements above the sea surface included instantaneous wave height estimates from laser and microwave altimeters; shortwave radiation; longwave radiation; and upwelling brightness temperature from radiometers; three more levels with sonic anemometers; a rain gauge; and multiple levels with relative humidity and temperature sensors. The data collected for this thesis relied primarily on these meteorological instruments located on the ASIT. More information on these instruments is listed in table 2.1 where T_{air} is air temperature, T_v is virtual temperature, RH is relative humidity, U is horizontal wind speed, P is pressure, and q_{air} is specific humidity (Edson, McGillis et al. 2003; Edson and McGillis 2003).

Table 2.1 Air-Sea Interaction Tower Meteorological Instruments

Instrument	Parameters	Approximate Height (m)	Sampling Rate (Hz)
Vaisala HMP45	T_{air}, RH, q_{air}	4, 6, 13, 16	1
Vaisala PTU	T_{air}, RH, q_{air}, P	8, 18	1
CSAT3	U, T_v, TKE, Fluxes	4, 6, 8, 16	20
Licor LI7000	q_{air}, Fluxes	13	20
Licor LI7500	q_{air}, Fluxes	4, 6, 8	20
Gill R2A	U, T_v, TKE, Fluxes	13	20
Gill R3A	U, T_v, TKE, Fluxes	18	20
Met3A	P, Fluxes	6, 8	8
Eppley PSP and PIR (Upward)	Downwelling Solar and IR Radiative Fluxes	22	1
Wintronics Radiometer (Downward)	SST, Upwelling IR Radiative Fluxes	11	1
Rain gauge	Rain	11	1
Riegl Laser altimeter	Wave Height Spectra	11	20
Microwave sensor	Wave Height Spectra	10	20
Profiling package	U, T_{air}, RH, q_{air}	3-14	1

2.4 Synoptic Situation

To assist in the interpretation of the measurements, the synoptic meteorological situation is investigated during the period of interest from August 20-27, 2003. The synoptic conditions are shown in figures 2.4a and b represented by various time series for this period measured at the ASIT. These time series are the sensible and latent heat fluxes were taken from the CSAT3 sonic anemometers and LI-7500 infrared hygrometer at 6 meters; temperature, specific and relative humidity were taken from the Vaisala HMP 45 probe at 6 meters; specific humidity, temperature (SST) of the sea surface, and upwelling IR were estimated from the downward facing Wintronics radiometer deployed at 11 meters; downwelling solar and infrared radiation measured from the upward facing Eppley PSP and PIR at 22 meters; wind direction (WD1-6) and horizontal wind speed (U1-6) where 1-6 annotate the heights 4, 6, 8, 13, 16, and 18 meters (see table 2.1 and figure 2.3 for instrument locations and sampling rates). Significant atmospheric events are annotated for correlation with surface meteorological plots and periods are numbered for a piecewise discussion. Note that the yeardays are marked in Greenwich Mean Time (GMT). The gaps in the wind data of figure 2.4b are a result of dropouts in the sonic data during periods of heaviest fog and rain. Periods when fog was present are annotated with black stars at the bottom of the composite plots. The criteria for fog at the ASIT that was used is as follows:

$$\left| T_{air} - T_{bb} \right| \le 6$$
$$q > q_s \tag{2.4.1}$$
$$RH \ge 95\%$$

where q and q_s are the specific humidities for air at 6 meters and sea surface respectively; RH is the relative humidity measured at 6 meters; T_{air} is measured at 6 meters and T_{bb} is the blackbody temperature defined as:

$$T_{bb} = \left(\frac{IR_{down}}{\sigma_{sb}} \right)^{-\frac{1}{4}} \tag{2.4.2}$$

27
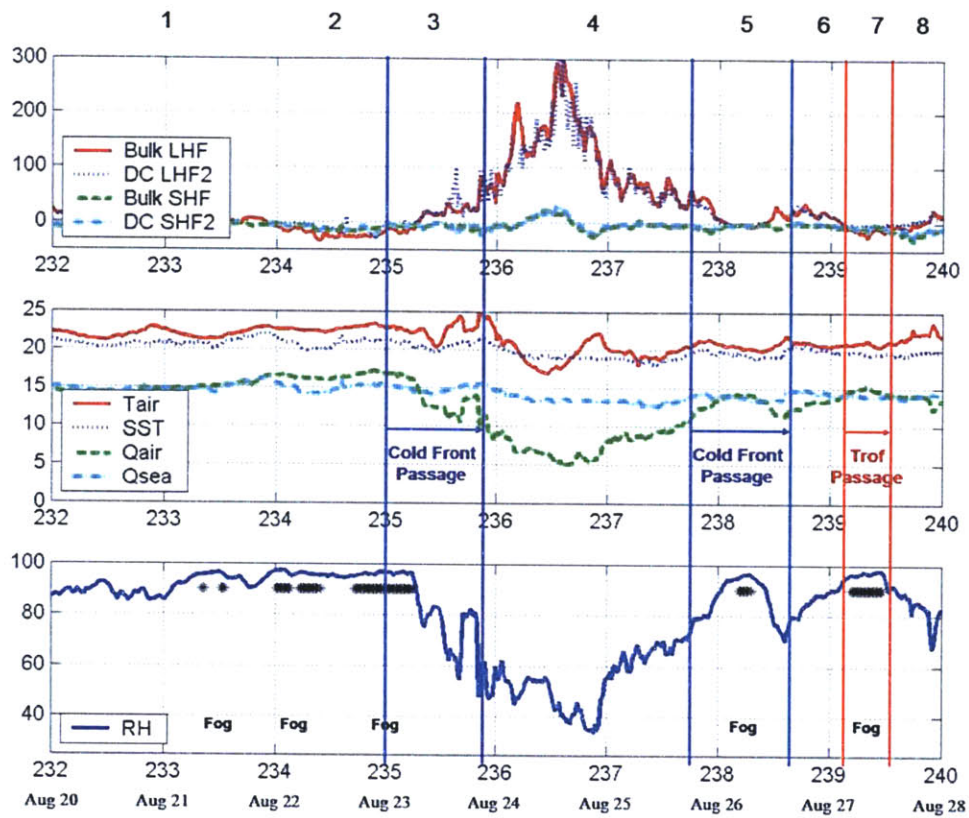
Figure 2.4a: Time series showing synoptic variability in sensible heat flux, latent heat flux (top panel); air-sea temperature and humidity differences (middle panel); and relative humidity (bottom panel). The lines denote significant synoptic events and the asterisks denote foggy conditions.
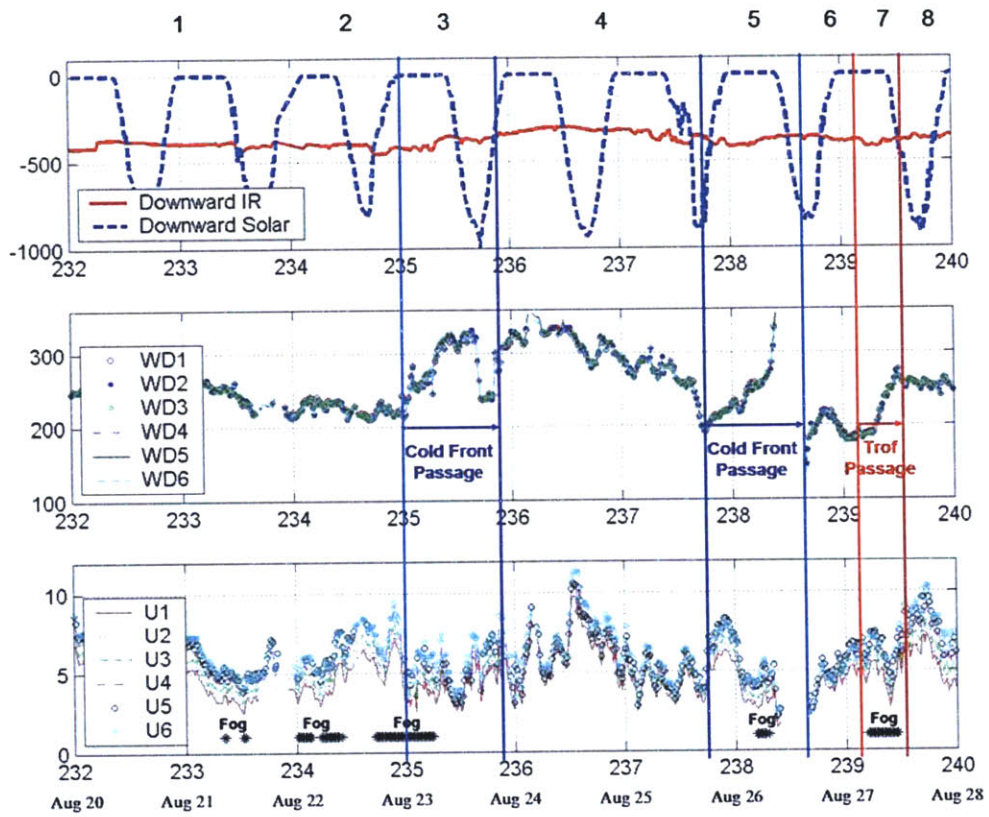
Figure 2.4b: As in figure 2.4a but for downwelling IR and solar radiation (top panel); wind direction (middle panel); and wind speed (bottom panel).

Figure 2.5 Parameters used to identify fog
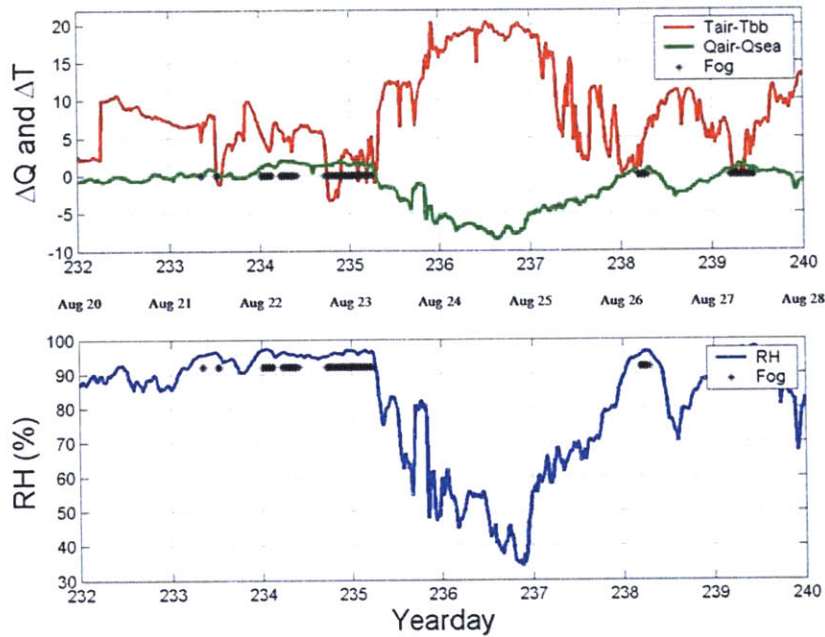
where $\sigma_{sb} = 5.67 \times 10^{-8}$ is the Stefan-Boltzmann constant and IR_{down} is the downwelling IR radiative flux measured at 22 meters. This criterion was achieved by matching known occurrences of fog based on visual observations, to the data. The standard measurement level of 6 meters was chosen to minimize distortion by the platform and the expectation that it was above the WBL for scalars. A plot of the criteria for fog formation is shown in figure 2.5. Temporal means of the measured parameters for each of the periods at a height of 6 meters are listed in table 2.1 at the end of this chapter. The data collection area consisting of the ASIT and MVCO will hereby be referred to as the data region.

Period 1 (figures 2.6a-d): This period was dominated by a high pressure system over the data region in mostly clear skies with periods of haze and light fog. It was warm and humid with light winds from the west-southwest. There was initially a weak trough off the coast of New England on the morning of the 20th which moved offshore as the day

Figure 2.6a 20 Aug 0800L
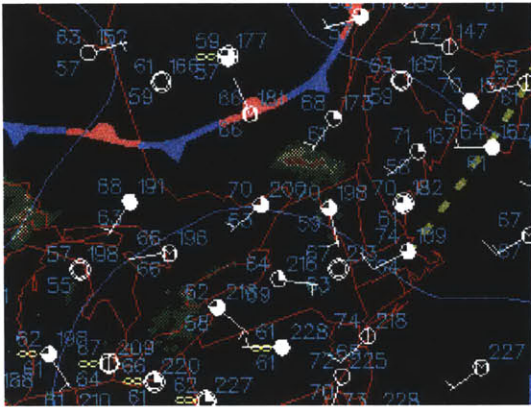
Figure 2.6b 20 Aug 2000L
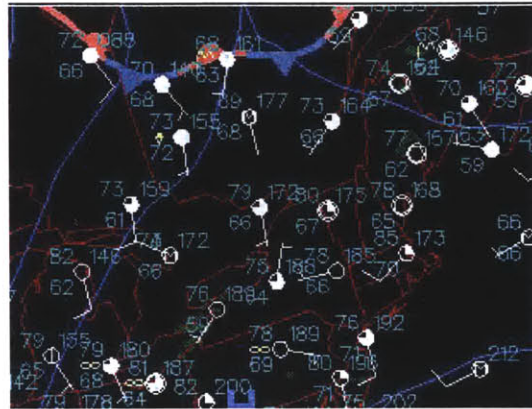
Figure 2.6c 21 Aug 0800L
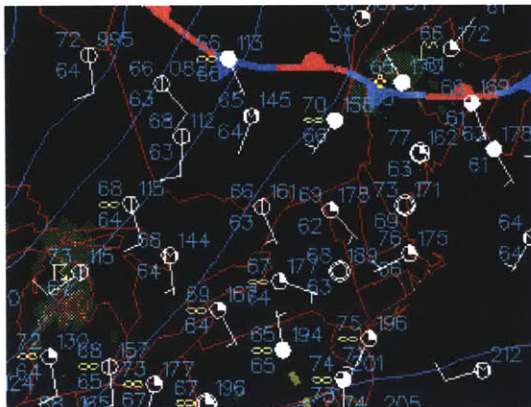
Figure 2.6d 21 Aug 2000L
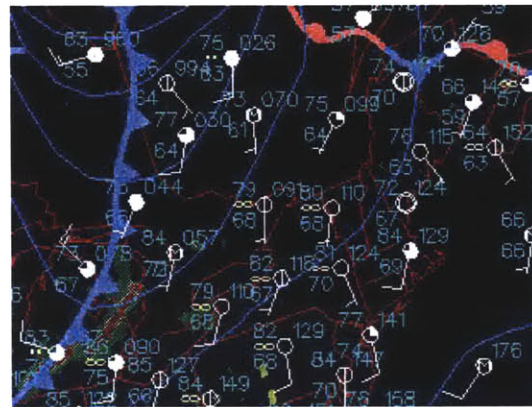
progressed. No local precipitation was produced by this trough. A stable boundary layer exists in this period and persists throughout the periods of interest.

Period 2 (figures 2.7a,b): During this period, the data region was in the warm sector of an approaching low pressure system resulting in warm temperatures with mostly hazy and foggy conditions throughout the period. Winds were light and from the southwest. The specific humidity of the sea was lower than that of the air and both the latent and specific heat fluxes were negative during this period.

Figure 2.7a 22 Aug 0800L
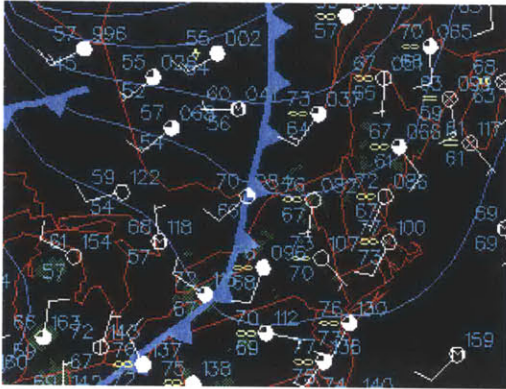
Figure 2.7b 22 Aug 2000L
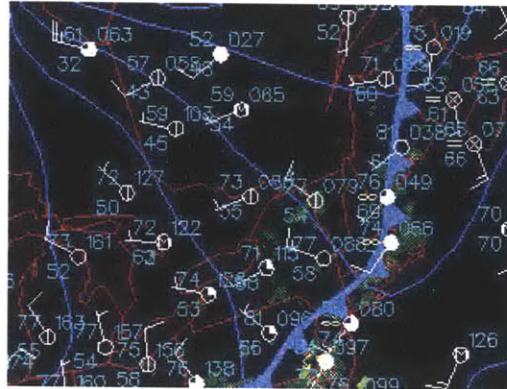
Period 3 (figures 2.8a,b): The passage of a cold front over the data region was evident by a pre-frontal shift of winds to the northwest followed by a post-frontal shift of winds to the southwest and the advection of drier air into the region. Skies went from partly cloudy to clear as the front progressed eastward with foggy conditions in the early morning hours of the 23rd. Winds were light and predominantly from the west-northwest. There was a slightly positive LHF during this period.

Figure 2.8a 23 Aug 0800L

Figure 2.8b 23 Aug 2000L
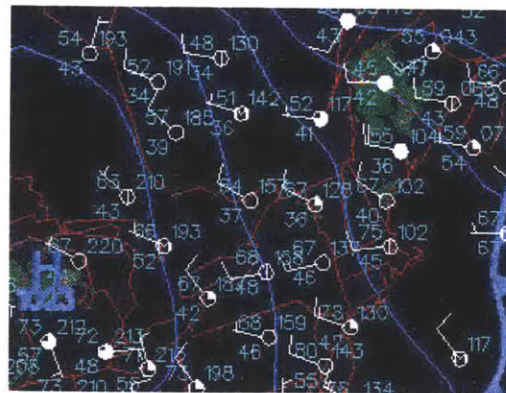
Period 4 (figures 2.9a-c): A high pressure system of relatively cool and very dry continental air from Canada resulted in clear, bright skies and a positive LHF. The specific humidity of the air was as much as 8.5 g/kg lower than that of the sea. The average specific heat flux (SHF) given in table 2.2 indicates stable conditions. However,

as shown by the time series in figure 2.4a, the period briefly displayed an interval of positive SHF and unstable conditions. Wind speed was slightly higher at around 10 m/s on the afternoon of the 24th but tapered off as the wind direction shifted from the north to the southwest as a new frontal system approached from the west.

Figure 2.9a 24 Aug 0800L
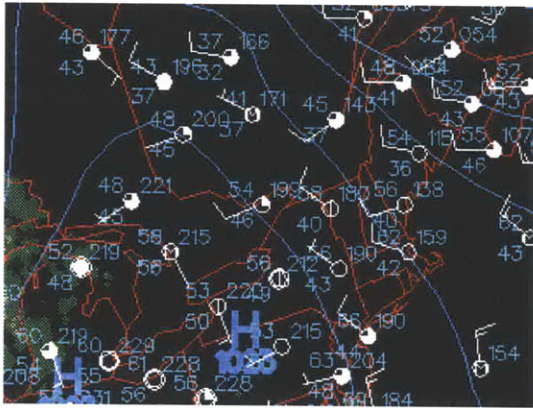
Figure 2.9b 24 Aug 2000L

Figure 2.9c 25 Aug 0800L
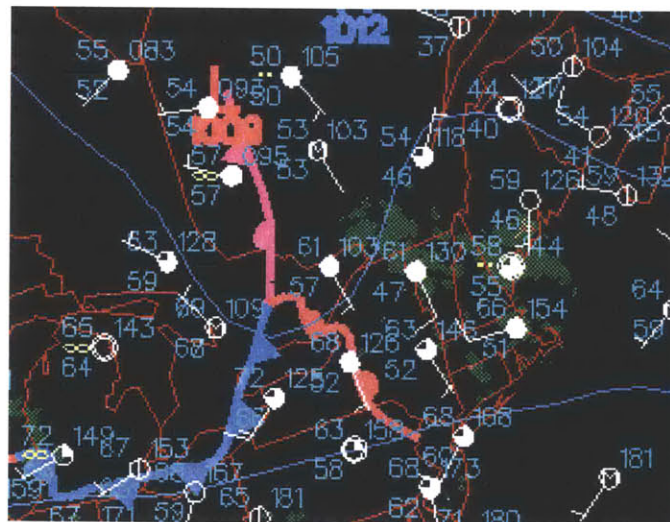
Period 5 (figures 2.10a,b): This period began with data region in the warm sector of another approaching low pressure system. Skies went from clear to mostly cloudy by the end of the period with the similar characteristic northerly and subsequent southerly

33

shift in the winds as the front passed. This front was not as strong as the previous front so the changes in temperature and specific humidity were not as pronounced. Nonetheless, conditions were sufficient to meet the criteria for fog formation in the early morning of the 26th.

Figure 2.10a 25 Aug 2000L
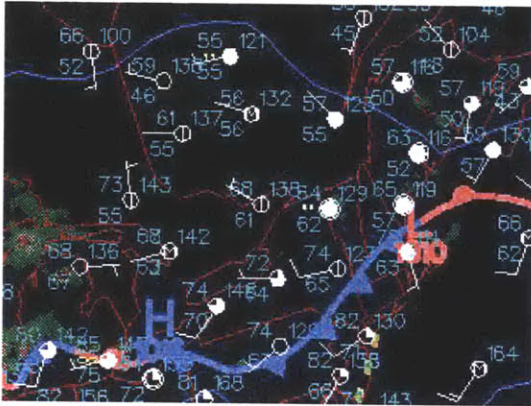
Figure 2.10b 26 Aug 0800L
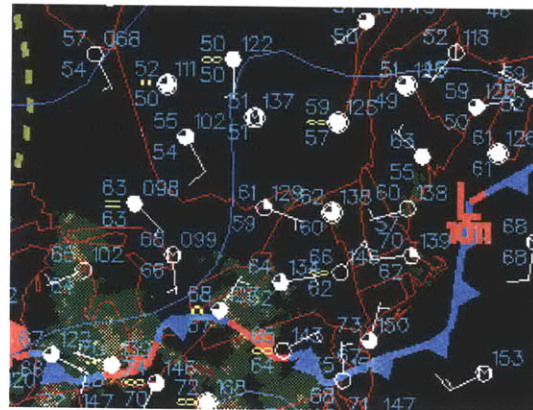
Period 6 (figure 2.11): During this period the data region was between the cold front which had recently passed over the region and the warm sector of another low pressure system to the north. Skies were partly cloudy with light winds from the south-southwest. Temperatures were warm with moderate humidity. There was a slightly positive LHF during this period.

Figure 2.11 26 Aug 2000L
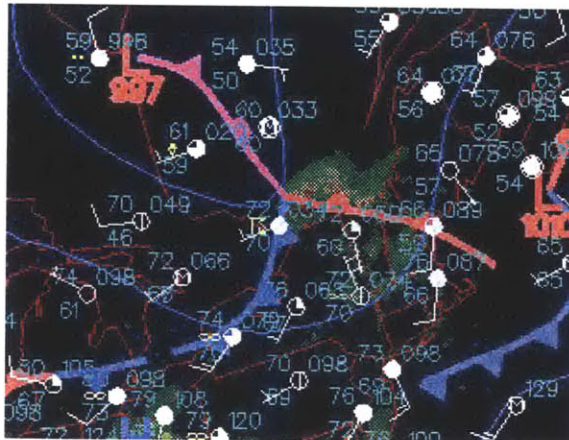
Period 7 (figure 2.12): During this period a trough passed over the data region. Winds shifted from the southwest to the west-northwest and were still relatively light. Conditions for fog were met late morning on the 27th and the rest of the period was characterized by partly cloudy skies.

Figure 2.12 27 Aug 0800L
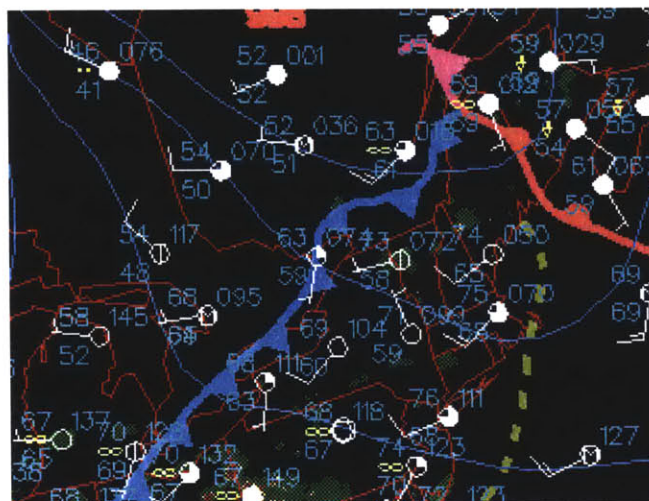
Period 8 (figure 2.13): This brief period at the end of the case study is characterized by an approaching cold front. Winds were between 5-10 m/s and from the west. Temperatures were warm with relatively mild humidity.

Figure 2.13 27 Aug 2000L
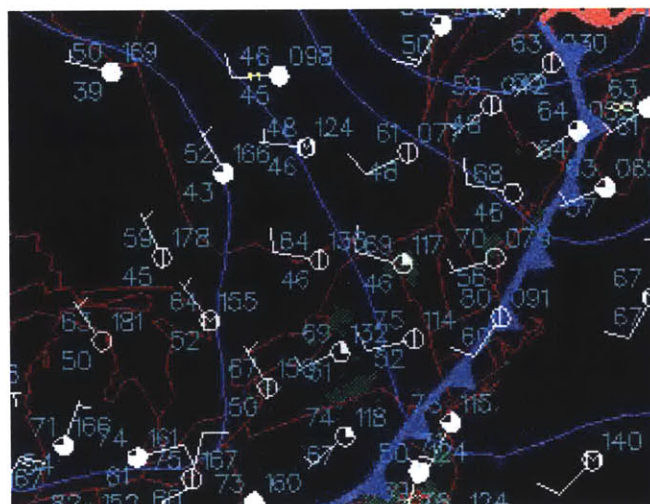
Table 2.2 Period Means

Parameter	1	2	3	4	5	6	7	8
T_{air} (C)	21.86	22.63	22.47	19.79	20.65	20.79	20.82	21.91
q_{air} (g/kg)	14.76	16.41	13.74	7.84	13.10	13.20	14.86	13.79
SST (C)	20.77	20.66	20.52	19.13	19.48	20.17	19.61	19.62
q_{sea} (g/kg)	14.89	14.89	14.81	13.50	13.81	14.45	13.99	13.98
LHF (W/ m^2)	4.06	-12.31	16.57	106.73	9.45	16.24	-4.12	3.87
SHF (W/ m^2)	-6.60	-11.91	-8.35	-1.04	-5.69	-1.44	-7.90	-13.61
RH (%)	90.77	95.71	81.01	54.73	86.90	86.28	96.51	84.16
U (m/s)	4.84	5.24	4.36	5.37	4.37	4.34	4.89	5.94
WD (°)	249.84	225.04	283.23	262.18	231.88	194.17	217.66	254.35

3. THEORY

3.1 Monin-Obukhov Similarity

Monin-Obukhov Similarity (MOS) is a statistical tool that was developed to study atmospheric turbulence in the surface layer over land and is sometimes referred to as surface-layer similarity (Monin and Obukhov 1954). The surface layer is defined as that part of the boundary layer where the fluxes vary by less than 10% and therefore MOS assumes a nearly constant flux layer. MOS also assumes that the statistics are stationary and horizontally homogenous. Within the boundary layer, and near the surface, turbulent energy is produced mainly by mechanical working of the stresses on the mean velocity gradient and higher up, principally by buoyant motions (Bradley, Coppin et al. 1991). The fluxes associated with these two production mechanisms are represented by the following:

$$u_* = \left[\frac{\bar{\tau}_s}{\rho_a}\right]^{\frac{1}{2}} = |F_u(0)|^{\frac{1}{2}} \tag{3.1.1}$$

$$\overline{w'\theta'_{v_s}} = \frac{Q_{h_s}}{\rho_a c_p} + 0.61 T_s \frac{Q_{e_s}}{\rho_a L_e} = F_\theta(0) + 0.61 T_s F_q(0) \tag{3.1.2}$$

where $\bar{\tau}_s$ is the stress vector at the surface (i.e., the surface stress), u_* is the friction velocity, Q_{h_s} is the surface value of the sensible heat flux, Q_{e_s} is the surface value of the LHF, T_s is the sea surface temperature (SST) and F_u, F_θ, and F_q are the kinematic forms of the momentum, sensible heat, and latent heat fluxes, at the surface respectively.

The friction velocity and heat fluxes are combined with the buoyancy parameter, $\frac{g}{\Theta_v}$, where g is the acceleration due to gravity and Θ_v is the mean virtual potential temperature; and the height above the surface, z, to form a set of scaling parameters for velocity, temperature, humidity and an additional length scale. The scaling parameters can be defined as:

37

$$x_* \equiv -\frac{F_x(0)}{u_*} \qquad (3.1.3)$$

where x_* is the respective scaling parameter for $x = q, \theta, u$. The additional length scale that results from a Buckingham-Pi analysis (Sabersky, Hauptmann et al. 1998) is known as the Obukhov length, L. The Obukhov length is proportional to the height at which buoyant production equals mechanical (shear) production of turbulence in a constant flux layer (2.3.1), and is expressed as:

$$L = -\frac{\Theta_v u_*^3}{g \kappa \overline{w'\theta'_{v_s}}} = \frac{\Theta_v u_*^2}{g \kappa \left(\theta_* + 0.61 T_s q_* \right)} \qquad (3.1.4)$$

The Obukhov length and height z are then combined to form the dimensionless parameter, ζ, called the surface layer scaling parameter:

$$\zeta = \frac{z}{L} = \frac{-\kappa z g \left(\overline{w'\theta'_v} \right)_s}{\overline{\theta_v} u_*^3} \qquad (3.1.5)$$

The sign of the surface layer scaling parameter relates to static stability: negative implies unstable conditions, and positive implies stable conditions.

The basis for MOS is that flows with similar ratios of convective to mechanical generation of turbulence at a given height (i.e similar ζ or Richardson numbers) should have similar statistical properties after normalization by the appropriate scaling parameters. Specifically, the similarity hypothesis states that normalization of surface layer variables by the appropriate scaling parameter(s) should be universal functions of the surface layer scaling parameter ζ. For example, using these scaling parameters, the TKE budget (2.3.1) can be normalized by $\frac{\kappa z}{u_*}$ to obtain:

$$\frac{\varepsilon \kappa z}{u_*^3} = \phi_\varepsilon(\zeta) = \phi_u(\zeta) - \zeta - \phi_{tp}(\zeta) - \phi_{te}(\zeta) \qquad (3.1.6)$$

where the ϕ functions represent the dimensionless form of the terms in (2.3.1). In a constant flux layer with no turning of the wind, the dimensionless gradient for velocity ϕ_u becomes:

38

$$\phi_u(\zeta) = \frac{\kappa z}{u_*} \frac{\partial U}{\partial z} \tag{3.1.7}$$

Likewise, the dimensionless gradients of specific humidity and potential temperature are;

$$\phi_q(\zeta) = \frac{\kappa z}{q_*} \frac{\partial Q}{\partial z}$$

$$\phi_\theta(\zeta) = \frac{\kappa z}{\theta_*} \frac{\partial \Theta}{\partial z} \tag{3.1.8}$$

where U, Q, and Θ are the mean values. As such MOS predicts that these non-dimensional gradients of velocity, humidity, and temperature are universal functions of atmospheric stability, ζ.

These relationships are commonly used to relate the fluxes to their respective profiles. For example, the combination of (3.1.3) with (3.1.7) and (3.1.8) results in the flux parameterization:

$$F_x = \overline{w'x'} = -u_* x_* = -\frac{u_* \kappa z}{\phi_x(\zeta)} \frac{\partial X}{\partial z} = -K_x \frac{\partial X}{\partial z} \tag{3.1.9}$$

where again, $x = q, \theta, u$, and K_x is the respective turbulent exchange coefficient. This is a first order, small eddy closure technique implying a down-gradient transport. These scaling laws are expected to hold and the derived parameterizations are expected to be universal as long as the assumptions that govern MOS laws are valid, i.e., a combination of mechanical and thermal forcing drive the turbulent exchange, the scaling parameters are independent of height in the surface layer, and the turbulence statistics are stationary and horizontally homogenous (Edson, Zappa et al. 2002; Stull 1988).

In the MABL, one can think of several situations where the assumptions governing MOS could become invalid. For example, very near the ocean surface, we expect to encounter a wave boundary layer (WBL) as described in section 1.2.2, where $U(t) = \overline{U} + u'(t) + \tilde{u}(t)$ and $\tilde{u}(t)$ represents the wave induced fluctuations in the velocity field. In such a flow field it is generally assumed that MOS is not valid since an additional forcing mechanism influences the near surface flow, i.e., the wave induced flow (Sullivan 2004; Edson, Zappa et al. 2002).

39

The primary question to be addressed in this thesis is whether or not MOS is valid in stable conditions. In the stable regime, the stratification begins to restrict the production of TKE through shear by limiting the size of the energy containing eddies (i.e. their velocity fluctuations). This is a result of the restoring forces that limit the displacement of the parcels from their equilibrium position. In extremely stable conditions, the size of the eddies are completely limited by the stability and they become unaware of their distance from the surface. The scaling becomes height independent under these conditions and the Monin-Obukhov (MO) length becomes the only length scale. As a result, we often refer to such conditions as z-less stratification (Welch, Ravichandran et al. 1986; Wyngaard, Busch et al. 1973). The weak and intermittent turbulence often observed in stable conditions, particularly in low wind conditions, leads to non-stationarity and inhomogeneity, which strongly impacts our ability to model the turbulent mixing of heat and water vapor. The processes controlling fog within the surface layer further complicate the parameterization of these fluxes (Gerber 1981).

3.2 TOGA COARE 3.0 Parameterization

The TOGA COARE 3.0 implementation of the bulk aerodynamic formula provides a starting point for this investigation. As stated earlier, TC 3.0 has been validated in several field programs characterized by unstable to near neutral conditions.

As opposed to the DC fluxes described in section 2.3, the bulk aerodynamic formula parameterize the kinematic fluxes in terms of the more easily measured mean or bulk quantities and are expressed:

$$Q_h = \rho_a c_{pa} C_H S (T_s - \theta)$$
$$Q_e = \rho_a L_e C_E S (q_s - q) \tag{3.2.1}$$
$$\tau_i = \rho_a C_D S (u_{si} - u_i)$$

where θ, q, u_i and S are the average potential temperature, specific humidity, horizontal wind velocity in the i th direction, and instantaneous wind speed, respectively, at some height z ; s denotes their surface values and C_H, C_E, and C_D are the transfer coefficients

for sensible heat (i.e. the Stanton number), latent heat (i.e. the Dalton number), and momentum (i.e. the drag coefficient) respectively. The interfacial value of the water vapor mixing ratio, q_s, is:

$$q_s = 0.98 q_{sat}(T_s) \qquad (3.2.2)$$

where the value of 0.98 multiplying the saturation specific humidity of the SST [$q_{sat}(T_s)$] takes into account the reduction in vapor pressure caused by a typical salinity of 34 parts per thousand. In this analysis, the potential temperature and specific humidity at reference height z_r are determined from:

$$\theta = T + 0.0098 z_r$$
$$q = RH q_{sat}(T) \qquad (3.2.3)$$

where RH is the relative humidity and T is the air temperature and 0.0098 K/m is the adiabatic lapse rate.

The use of S in equations (3.2.1) is an important point explained in the following excerpt from Edson (2003). As buoyant production begins to dominate the generation of turbulence in a very unstable (convective) atmospheric boundary layer, the mean wind vector, U, and the mean shear, $\dfrac{\partial U}{\partial z}$, approach zero. However, the variance of the velocity components and instantaneous shear remain finite due to the convective motion that drives eddies capable of transporting heat and momentum. The size of these eddies scales with the boundary layer depth and the strength of the buoyancy flux, and define a convective velocity scale given by:

$$w_* = \left(\frac{g}{\theta_v} \overline{w'\theta_v'} z_i \right)^{\frac{1}{3}} \qquad (3.2.4)$$

The TC 3.0 bulk algorithm attempts to account for the heat and momentum exchange driven by these convective eddies by modifying the traditional definition of the bulk formula to include the mean instantaneous wind speed:

$$S = \overline{\left(u_{rx}^2 + u_{ry}^2 + u_z^2 \right)^{\frac{1}{2}}} \qquad (3.2.5)$$

41

where the subscript r denotes that the values are relative to the sea surface.

Unfortunately, it is not always possible to accurately measure the mean wind speed over the ocean due to platform motion. For example, the mean wind speed measured from a buoy mounted cup anemometer will include fluctuations from both the wind and wave induced motions. For this reason, the mean wind components (i.e., vector averaged winds) are normally measured on ships and buoys because the sinusoidal nature of the wave induced motions tend to average out. The following definition is then used to estimate the wind speed from the mean wind components:

$$S = \overline{\left(u_{rx}^2 + u_{ry}^2 + u_z^2\right)^{\frac{1}{2}}} = \left(\overline{u}_{rx}^2 + \overline{u}_{ry}^2 + w_g^2\right)^{\frac{1}{2}} \tag{3.2.6}$$

where w_g is known as the gustiness and provides an estimate of the wind speed measurements of the mean wind vector. The gustiness is related to the convective velocity by:

$$w_g = \beta w_* \tag{3.2.7}$$

where β is a numerical constant known as the gustiness parameter with a value of order 1. Fortunately for this study, the fixed sensors on the ASIT allow direct measurement of S.

The parameterization of the transfer coefficients begins with commonly used forms of the diabatic profiles found through integration of (3.1.7). This provides the mean quantities at height z:

$$U(z) = \frac{u_*}{\kappa}\left[\ln\left(\frac{z}{z_o}\right) - \psi_u(\zeta)\right]$$

$$\theta(z) = \frac{\theta_*}{\kappa}\left[\ln\left(\frac{z}{z_\theta}\right) - \psi_\theta(\zeta)\right] \tag{3.2.8}$$

$$Q(z) = \frac{q_*}{\kappa}\left[\ln\left(\frac{z}{z_q}\right) - \psi_q(\zeta)\right]$$

where the stability parameter ψ_x is defined as:

$$\psi_x(\zeta) = \int_0^\zeta \frac{\left(1 - \phi_x(\zeta)\right)}{\zeta} d\zeta \tag{3.2.9}$$

42

and $z_{o,\theta,q}$ are the roughness lengths for momentum, heat, and moisture respectively. The roughness lengths are defined as the height where the extrapolation of the log-z portion of the respective profile intersects the surface value. The most commonly used forms of the dimensionless gradient functions are known as the Businger-Dyer formulations and are given by:

$$
\left.\begin{array}{l}
\phi_u = 1 + C_1 \zeta \\
\phi_\theta = \phi_q = 1 + C_2 \zeta
\end{array}\right\} \qquad 0 < \zeta < 0.2
$$

$$
\left.\begin{array}{l}
\phi_u = \left(1 + C_3 \zeta\right)^{-\frac{1}{4}} \\
\phi_\theta = \phi_q = \left(1 + C_4 \zeta\right)^{-\frac{1}{2}}
\end{array}\right\} \qquad -1 < \zeta < 0
$$

(3.2.10)

where C_H are the numerical coefficients found from field experiments. Decades of overland experiments have resulted in a range of values. However, commonly used values are given by $C_1 = C_2 = 5$ and $C_3 = C_4 = 16$, which can be combined with (3.2.9) to define the stability parameters:

$$
\psi_u (\zeta) = \psi_\theta (\zeta) = \psi_q (\zeta) = 5\zeta \left.\right\} \qquad \text{stable} \qquad (3.2.11)
$$

$$
\left.\begin{array}{l}
\psi_u (\zeta) = 2\ln\left[\dfrac{1 + \left(1 - 16\zeta\right)^{-\frac{1}{4}}}{2}\right] + \ln\left[\dfrac{1 + \left(1 - 16\zeta\right)^{-\frac{1}{2}}}{2}\right] - 2\tan^{-1}\left(1 - 16\zeta\right)^{-\frac{1}{4}} + \dfrac{\pi}{2} \\[2em]
\psi_\theta (\zeta) = \psi_q (\zeta) = 2\ln\left[\dfrac{1 + \left(1 - 16\zeta\right)^{-\frac{1}{2}}}{2}\right]
\end{array}\right\} \text{unstable (3.2.12)}
$$

(Paulson 1970; Large and Pond 1982):

The TC 3.0 algorithm partitions the transfer coefficients into individual profile components:

$$
\begin{array}{l}
C_H = c_\theta^{\frac{1}{2}} c_D^{\frac{1}{2}} \\
C_E = c_q^{\frac{1}{2}} c_D^{\frac{1}{2}} \\
C_D = c_D^{\frac{1}{2}} c_D^{\frac{1}{2}}
\end{array}
$$

(3.2.13)

The combination of (3.2.13) with (3.2.1) and (3.2.8) yields the following semi-empirical forms of these components:

$$c_\theta^{\frac{1}{2}} = \frac{a\kappa}{\left[\ln\left(\dfrac{z}{z_\theta}\right) - \psi_\theta(\zeta)\right]}$$

$$c_q^{\frac{1}{2}} = \frac{a\kappa}{\left[\ln\left(\dfrac{z}{z_q}\right) - \psi_q(\zeta)\right]} \tag{3.2.14}$$

$$c_D^{\frac{1}{2}} = \frac{\kappa}{\left[\ln\left(\dfrac{z}{z_o}\right) - \psi_u(\zeta)\right]}$$

where a accounts for the difference in scalar and velocity von Kármán constants. The neutral transfer coefficients defined by $\zeta = 0$ and $\psi_x = 0$ are related to these transfer coefficients through (Large and Pond 1982):

$$c_{\theta n}^{\frac{1}{2}} = \frac{a\kappa}{\ln\left(\dfrac{z_r}{z_\theta}\right)} = \frac{c_\theta^{\frac{1}{2}}}{1 + \dfrac{c_\theta^{\frac{1}{2}}}{a\kappa}\psi_\theta(\zeta)}$$

$$c_{qn}^{\frac{1}{2}} = \frac{a\kappa}{\ln\left(\dfrac{z_r}{z_q}\right)} = \frac{c_q^{\frac{1}{2}}}{1 + \dfrac{c_q^{\frac{1}{2}}}{a\kappa}\psi_q(\zeta)} \tag{3.2.15}$$

$$c_{Dn}^{\frac{1}{2}} = \frac{\kappa}{\ln\left(\dfrac{z_r}{z_o}\right)} = \frac{c_\theta^{\frac{1}{2}}}{1 + \dfrac{c_D^{\frac{1}{2}}}{\kappa}\psi_u(\zeta)}$$

The MOS scalar scaling parameters can be computed independently from the velocity measurements:

$$\theta_* = -c_\theta^{\frac{1}{2}}\left(T_s - \theta\right)$$
$$q_* = -c_q^{\frac{1}{2}}\left(q_s - q\right) \tag{3.2.16}$$

The ability to compute the scalar components separately is advantageous because the drag coefficient is sensitive to both sea state and wave age, while the scalar coefficients

may be influenced by additional processes such as wave breaking and heat exchange from evaporating sea spray (Edson, Zappa et al. 2002).

Because the transfer coefficients are functions of height and stability it is common practice to adopt a reference height of 10m and adjust profiles to their form at neutral stability to compare results from different elevations. The expression "neutral transfer coefficient" is a classic contradiction in terms, since neutral stability implies zero heat flux at the surface and a nonexistent potential temp gradient (Bradley, Coppin et al. 1991). In addition to neutral transfer coefficients, the neutral wind speed is found from:

$$U_N = U_r^{\frac{1}{2}} S^{\frac{1}{2}} + \frac{\psi_u(\zeta) u_*}{\kappa} = U_r^{\frac{1}{2}} \left(U_r^2 + w_g^2\right)^{\frac{1}{4}} + \frac{\psi_u(\zeta) u_*}{\kappa} \qquad (3.2.17)$$

The velocity roughness length z_o is often related to the viscous sub layer at low winds and the physical roughness of the surface at higher winds. The scalar roughness lengths are related to the thermal sub layer. It has proven convenient to characterize the surface and the flow regime by the roughness Reynolds number:

$$R_r = \frac{u_* z}{v} \qquad (3.2.18)$$

As the wind speed decreases, laboratory experiments have shown that R_r approaches a constant value of about 0.11 and the relationship between roughness and stress is given by:

$$z_o = \frac{0.11 v}{u_*} \qquad (3.2.19)$$

The validity of this smooth flow relationship at low winds over a malleable ocean surface (i.e, its surface characteristics are also governed by surface tension) remains a matter of some debate for field applications.

The relationship between oceanic roughness and stress for rough flow is:

$$z_o = \frac{\alpha u_*^2}{g} \qquad (3.2.20)$$

where α is the Charnock constant which has values between 0.010 and 0.035 and is linked to gross characterizations of the sea state such as wave age or slope of the

45

dominant wavelength (from the peak of the gravity wave spectrum). Combining (3.2.19) and (3.2.20) we get a more comprehensive expression for z_o (Smith 1988; Fairall, Bradley et al. 1996):

$$z_o = \frac{\alpha u_*^2}{g} + \frac{0.11\nu}{u_*} \tag{3.2.21}$$

The dependence of the Charnock "variable" as a function of sea state is the focus of many ongoing investigations

3.3 Local Similarity

In section 3.1, a condition referred to as z-less stratification is described for the stable regime as the condition when the buoyancy force begins to restrict the production of TKE through shear by limiting the size of the energy containing eddies, i.e. their velocity fluctuations. In other words, local similarity (LS) recognizes that turbulence in the mid and upper stable MABL may not be in equilibrium with the surface fluxes. This means that the local fluxes, shears and stability are more important than the surface values. For comparison, the orders of magnitude for MOS scaling factors in unstable conditions are:

$$L \qquad \sim O\left(1m - 200m\right)$$

$$z \qquad \sim O\left(0.01m - 0.1z_i m\right)$$

$$u_* \qquad \sim O\left(0.05\frac{m}{s} - 0.3\frac{m}{s}\right)$$

$$\theta_* \qquad \sim O\left(0.1^\circ C - 2.0^\circ C\right)$$

$$q_* \qquad \sim O\left(0.1\frac{g}{kg} - 5\frac{g}{kg}\right)$$

while for LS, the relevant scales are:

$$L(z) \qquad \sim O(0m - 50m)$$

$$u_*(z) \qquad \sim O(0m/s - 0.3m/s)$$

$$\theta_*(z) \qquad \sim O(-2.0°C - 0°C)$$

$$q_*(z) \qquad \sim O(-2g/kg - 5g/kg)$$

Dimensionless groups formed from these scales are not functions of height z, although the individual scaling variables listed above may vary significantly with height (Stull 1988). These LS scaling factors are computed as:

$$u_L = u_*(z)$$

$$L_L = \frac{\Theta_v u_L(z)^3}{g\kappa \overline{w'\theta_v'(z)}}$$

$$\theta_L = -\frac{\overline{w'\theta_v'(z)}}{u_L(z)} \qquad (3.3.1)$$

$$q_L = -\frac{\overline{w'q'(z)}}{u_L(z)}$$

where L_L is the only length scale.

In conditions of z-less stratification, the velocity, temperature, and humidity gradients are proportional to $\dfrac{x_*}{L_L}$, i.e:

$$\frac{\partial X}{\partial z} \propto \frac{x_*}{L_L} \qquad (3.3.2)$$

and therefore:

$$\phi_x = \frac{\kappa z}{x_*}\frac{\partial X}{\partial z} \propto \frac{\kappa z}{x_*}\frac{x_*}{L_L} \propto \frac{z}{L_L} \qquad (3.3.3)$$

Most experiments show that in stable conditions the following is true:

$$\phi_x = 1 + \beta\frac{z}{L} \qquad (3.3.4)$$

which is the same as equations (3.2.10) with $\beta = C_{\#}$ (Wyngaard, Busch et al. 1973).

All of these relationships assume that the stable MABL is continuously turbulent in time and space with no gaps or patches of nonturbulent air. Since real stable MABLs have sporadic, patchy turbulence, it is important to recognize that these expressions have their limitations (Stull 1988).

3.4 Enthalpy and Specific Enthalpy

To determine our best estimates of the DC fluxes for comparison with the TC 3.0 parameterizations of the scalar transfer coefficients, we examine the enthalpy exchange of the system. The following discussion of enthalpy is from Edson (2004) based on the work of Businger (1982) and Webb et al. (1980). Enthalpy is a combination of the latent and specific heat fluxes and therefore the exchange of enthalpy is of paramount significance in representing an estimate of the total energy entering a system. As a result, care should be taken to use consistent forms of the sensible and latent heat fluxes to ensure that enthalpy is conserved. Through a detailed investigation of the enthalpy exchange in stable conditions with and without fog, we hope to gain valuable insights that will point to possible sources for error in the TC 3.0 parameterizations. This discussion presents the traditional equations for enthalpy and then discusses correction factors that may be included in the equations to account for internal energy changes due to the presence of water vapor and an additional correction for the presence of liquid water droplets. Ideally, the addition of the correction factors and the correction for the presence of liquid water droplets should improve the accounting for the complex energy exchanges associated with fog in the MABL.

3.4.1 Traditional Equations

We begin with the traditional equations defining enthalpy from Emanuel (1995):

$$k_d = c_{pd}T \tag{3.4.1}$$

$$k_w = c_{pw}T \tag{3.4.2}$$

$$k_v = c_{pv}T = k_w + L_e = c_{pw}T + L_e \tag{3.4.3}$$

where k_d, k_v, k_w and c_{pd}, c_{pv}, c_{pw} are the specific enthalpy and specific heat at constant pressure of dry air, water vapor, and liquid water, respectively; and T is the temperature of these constituents.

Even if no fog or sea spray is present in the MABL, there is still moisture present. So we begin with the equation for specific enthalpy of moist air just above the surface as defined by Emanuel (1995) using equations (3.4.1), (3.4.2) and (3.4.3):

$$k_m = (1-q)c_{pd}T + qc_{pv}T \tag{3.4.4}$$

or

$$k_m = (1-q)c_{pd}T + q\left(c_{pw}T + L_e\right) \tag{3.4.5}$$

Using (3.4.5) and the expansion described by Businger (1982) we can derive the surface enthalpy flux as:

$$\overline{\rho w k_{m_s}} \approx \overline{\rho}\,\overline{w'T'}\left[(1-\overline{q})c_{pd} + \overline{q}c_{pv}\right] + \overline{\rho}\,\overline{w'q'}\left[c_{pw}\overline{T} + L_e\right] \tag{3.4.6}$$

3.4.2 System Enthalpy

To investigate the enthalpy carried by a parcel of air and how it impacts the enthalpy of the system away from the surface, Businger (1982) included a set of arbitrary constants in the equations for enthalpy as follows:

$$k_d = c_{pd}T + b_d \tag{3.4.7}$$

$$k_v = c_{pv}T + b_v = k_w + L_e \tag{3.4.8}$$

$$k_w = c_{pw}T + b_w \tag{3.4.9}$$

where b_d, b_v, b_w are constants which are dependant upon the internal energies of these constituents. The latent heat of vaporization, L_e, is not considered a constant here, but a function of temperature, $L_e(T)$.

49

Using equations (3.4.7), (3.4.8), and (3.4.9) we obtain the following expressions for specific enthalpy of moist air:

$$k_m = (1-q)c_{pd}T + qc_{pv}T + b_{m1} \qquad (3.4.10)$$

or

$$k_m = (1-q)c_{pd}T + qc_{pw}T + qL_e + b_{m2} \qquad (3.4.11)$$

where

$$b_{m1} = (1-q)b_d + qb_v \qquad (3.4.12)$$

$$b_{m2} = (1-q)b_d + qb_w \qquad (3.4.13)$$

Now an enthalpy flux can be derived using (3.4.11) and (3.4.13) as follows:

$$\overline{\rho w k_m} = \overline{\rho w(1-q)c_{pd}T} + \overline{\rho w q c_{pw}T} + \overline{\rho w q L_e} + \overline{\rho w b_{m2}} \qquad (3.4.14)$$

on which an expansion is performed based on Businger (1982) but modified by Edson (2004) to be consistent with the results of Webb et al. (1980) to obtain (see Appendix A):

$$\overline{\rho w k_m} = \overline{\rho} \, \overline{w'T'} \left[(1-\overline{q})c_{pd} + \overline{q}c_{pv} \right] + \frac{\overline{\rho}}{(1-\overline{q})} \overline{w'q'} \left[c_{pw}\overline{T} + \overline{L}_e + b_w \right] \qquad (3.4.15)$$

As Businger (1982) describes, the combination of constants with the specific humidity in the previous expressions are necessary because the source of the water vapor in a parcel of air may have different initial conditions. Since the sea surface is the primary source of water vapor in the MABL even in the absence of sea-spray or fog, one needs to consider the specific enthalpy between the sea surface and the water vapor at the surface. Businger (1982) asserts that this is equivalent to the expression:

$$b_w = -c_{pw}\overline{T}_o \qquad (3.4.16)$$

where $\overline{T}_o$ is the average sea surface temperature. This closes the expression for the moist enthalpy flux in the surface layer, and provides an expression for the enthalpy flux away from the surface:

$$\overline{\rho w k_m} \approx \overline{\rho} \, \overline{w'T'} \left[(1-\overline{q})c_{pd} + \overline{q}c_{pv} \right] + \frac{\overline{\rho}}{(1-\overline{q})} \overline{w'q'} \left[c_{pw}\left(\overline{T}-\overline{T}_o\right) + \overline{L}_{e_n} \right] \qquad (3.4.17)$$

Alternatively, we can use the relationship $\overline{L_{e_n}} - \overline{L_e} = (c_{pv} - c_{pw})(\overline{T} - \overline{T_o})$ to obtain:

$$\overline{\rho w k_m} \approx \overline{\rho w'T'}\left[(1-\overline{q})c_{pd} + \overline{q}c_{pv}\right] + \frac{\overline{\rho}}{(1-\overline{q})}\overline{w'q'}\left[c_{pv}(\overline{T}-\overline{T_o}) + \overline{L_e}\right] \qquad (3.4.18)$$

which is Eq.(17) in Businger (1982) and is consistent with Eq.(39) in Webb et al. (1980). As explained in Fairall et al. (1996), the surface temperature in equation (3.4.17) represents the heat required to cool the water vapor from its initial temperature $\overline{T_o}$ to the air temperature $\overline{T}$ for unstable conditions. Webb et al. (1980) describe this term by noting that the heat imparted to and carried by the air parcel is represented by the change in temperature $(\overline{T} - \overline{T_o})$, not the temperature itself.

With these correction factors, the total SHF is represented as:

$$Q_h = \overline{\rho w'T'}\left[(1-\overline{q})c_{pd} + \overline{q}c_{pv}\right] + \frac{\overline{\rho}}{(1-\overline{q})}\overline{w'q'}c_{pv}(\overline{T}-\overline{T_o}) \qquad (3.4.19)$$

which is identical to the leading two terms in Eq.(39) given by Webb et al. (1980). The remaining components represent the total LHF:

$$Q_e = \frac{\overline{\rho}}{(1-\overline{q})}\overline{L_e}\overline{w'q'} = \overline{L_e}\left(\overline{w'\rho_v'} + \overline{w}\overline{\rho_v}\right) \qquad (3.4.20)$$

where

$$\overline{w} = 1.61\frac{\overline{w'\rho_v'}}{\overline{\rho_a}} + \left(1 + 1.61\frac{\overline{q}}{1-\overline{q}}\right)\frac{\overline{w'T'}}{\overline{T}} \qquad (3.4.21)$$

Equation (3.4.20) is identical to Eqs.(23) and (25) in Webb et al. (1980).

Using these expressions for enthalpy and enthalpy flux, it is now possible to define the enthalpy coefficient C_K as follows:

$$C_K = c_K^{\frac{1}{2}}c_D^{\frac{1}{2}} \qquad (3.4.22)$$

where

$$c_K^{\frac{1}{2}} = -\frac{k_*}{\left(k_{m_s} - k_m\right)} \qquad (3.4.23)$$

and

$$k_* = -\frac{\overline{\rho w k_m}}{u_*} \tag{3.4.24}$$

where k_{m_s} is the specific enthalpy of the sea surface. Additionally, we can define the dimensionless enthalpy flux as follows:

$$\phi_k = \frac{\kappa z}{k_*} \frac{\partial k_m}{\partial z} \tag{3.4.25}$$

and

$$\frac{\partial k_m}{\partial z} = \left(c_{pd} - q c_{pd} + q c_{pv} \right) \frac{\partial T}{\partial z} + \left[\left(T - T_o \right) c_{pw} - c_{pd} T + L_e \right] \frac{\partial q}{\partial z} \tag{3.4.26}$$

which was derived from (3.4.11) using $b_{m2} = b_w = -c_{pw} T_o$ such that:

$$\overline{k}_m = \left(1 - \overline{q} \right) c_{pd} \overline{T} + \overline{q} \left[c_{pw} \left(\overline{T} - \overline{T}_o \right) + \overline{L}_e \right] \tag{3.4.27}$$

3.4.3 Inclusion of Liquid Water

In fog, there are liquid water droplets present in the air in addition to water vapor. The discussion of enthalpy thus far only accounts for the effects of water vapor on the net enthalpy flux and does not consider the effects of liquid water droplets. Therefore, we now consider the effects of liquid water on the net enthalpy flux. We start with an expression from Frank and Emmitt (1981) for the specific enthalpy of moist air that includes liquid water:

$$k_m = \left(1 - q - q_w \right) k_d + q k_v + q_w k_w \tag{3.4.28}$$

or

$$k_m = \left(1 - q - q_w \right) k_d + \left(q + q_w \right) k_w + q L_e \tag{3.4.29}$$

where q_w is the specific enthalpy of liquid water. The moist enthalpy is then given by:

$$k_m = \left(1 - q - q_w \right) c_{pd} T + \left(q + q_w \right) c_w T + q L_e + b_{m3} \tag{3.4.30}$$

where

$$b_{m3} = \left(1 - q - q_w \right) b_d + \left(q + q_w \right) b_w \tag{3.4.31}$$

From (3.4.30) the moist enthalpy flux including liquid water is:

$$\overline{\rho w k_m} = \overline{\rho w (1-q-q_w) c_{pd} T} + \overline{\rho w (q+q_w) c_{pw} T} + \overline{\rho w q L_e} + \overline{\rho w b_{m3}} \qquad (3.4.32)$$

Using equation (3.4.32) and the expansion given in Appendix B, we obtain an estimate of the moist enthalpy flux including liquid water;

$$\overline{\rho w k_m} = \overline{\rho} \overline{w'T'} \left[(1-\overline{q}-\overline{q}_w) c_{pd} + \overline{q} c_{pv} + \overline{q}_w c_{pw} \right] + \frac{\overline{\rho}}{(1-\overline{q}-\overline{q}_w)} \left(\overline{w'q'} + \overline{w'q'_w} \right) \left[c_{pw} (\overline{T} - \overline{T}_o) + \overline{L}_{e_o} \right] (3.4.33)$$

The sensible and latent heat fluxes then become:

$$Q_h = \overline{\rho} \overline{w'T'} \left[(1-\overline{q}-\overline{q}_w) c_{pd} + \overline{q} c_{pv} + \overline{q}_w c_{pw} \right] + \frac{\overline{\rho}}{(1-\overline{q}-\overline{q}_w)} \left[\overline{w'q'} + \overline{w'q'_w} \right] c_{pw} (\overline{T} - \overline{T}_o) (3.4.34)$$

$$Q_e = \frac{\overline{\rho}}{(1-\overline{q}-\overline{q}_w)} L_{v_o} \left(\overline{w'q'} + \overline{w'q'_w} \right) \qquad (3.4.35)$$

where the liquid water content in typical marine fog is $q_w = 0.05 - 0.1 \frac{\text{g}}{\text{m}^3}$ (Wallace and

Hobbs 1977) and $\overline{w'q'_w}$ is the liquid water flux.

Equations (3.4.34) and (3.4.35) for the SHF and LHF respectively appear to represent a full accounting for water vapor and liquid water in the air. If these equations are incorporated into the TC 3.0 parameterizations, one would expect that a more accurate estimate of the sensible and latent heat fluxes would be achieved not only for stable conditions, but stable conditions with fog as well. The next chapter will investigate this premise and attempt to close the error gaps between TC 3.0 and DC measurements under these conditions.

4. RESULTS AND DISCUSSION

4.1 Transfer Coefficients

We now return to the question as to whether MOS is valid for parameterizing scalar fluxes in stable conditions with fog. Due to the efforts of scientists through the various field experiments listed in section 1.1, we know that MOS works well in unstable conditions where turbulence is driven by buoyancy and shear (Edson 2004). In contrast, the applicability of MOS in strongly stratified boundary layers remains an open question. Our poor understanding of the stratified boundary layers has motivated several recently completed overland field experiments to investigate this and other questions (Poulos, Blumen et al. 2002). In addition, the effects of fog on the net enthalpy exchange between the ocean and the atmosphere are not well known due to the sparseness of data collected under these conditions. Fortunately, the data collected during the case study period of August 20-27, 2003 contains measurements in stable conditions with fog and should allow us to investigate this issue to an unprecedented degree of detail.

To begin the examination of the data acquired during the case study period, we return to the MOS based TC 3.0 bulk equations (3.2.1). By inspection, unknowns in the bulk parameterizations are the transfer coefficients C_E and C_H which can be calculated by equations (3.2.13) and (3.2.14). Therefore, the proper parameterization of these coefficients is essential to the accuracy by which the TC 3.0 bulk equations can predict the SV fluxes.

4.2 Moisture Corrections

Figures 4.1 through 4.6 are plots of the neutral values of C_E, C_H and C_K corrected to 10 meters versus the neutral value of the mean horizontal wind component corrected to 10 meters are shown in the top panels. The lower panels show the ϕ_q, ϕ_θ, and ϕ_k versus stability with no fog present as calculated with equations (3.2.13), (3.2.14), (3.2.15) and

(3.1.7), (3.1.9) respectively. The foggy conditions have been removed using the criteria developed in section 3. The direct covariance fluxes used to calculate the transfer coefficients and the dimensionless fluxes were calculated using the equations for the latent and specific heat fluxes (3.4.19) and (3.4.20) as described in section 3.4.2 by Businger (1982).

The plots show a comparison of the direct covariance values versus the TC 3.0 values. The accuracy of the TC 3.0 parameterizations for the neutral transfer coefficients in both unstable and stable conditions with no fog present can be seen in the upper panels of figures 4.1, 4.3, and 4.5. The bottom panels are the means and standard deviations for stable conditions only. Since the dimensionless profile functions are functions of $\frac{z}{L}$, it makes sense to describe the ability of TC 3.0 in parameterizing the fluxes by looking at the unstable and stable conditions separately. In unstable conditions with no fog present, TC 3.0 performs reasonably well in parameterizing all of the transfer coefficients. The Dalton number is nearly prefect in unstable conditions as can be seen in figure 4.1. The Stanton number is only slightly overestimated in unstable conditions as can be seen in figure 4.3. Figure 4.5 shows that TC 3.0 slightly underestimates the enthalpy coefficient in unstable conditions. The behavior of the dimensionless flux parameterizations in unstable conditions are good as well. There is very good agreement for ϕ_q and ϕ_θ in figures 4.2 and 4.4. In figure 4.6, we see that TC 3.0 slightly overestimates ϕ_k. Despite, these minor differences, these plots validate the conclusions of recent field studies that the TC 3.0 parameterizations work remarkably well in unstable conditions. Additionally, ongoing investigations to improve the calibration of the LI-7500 indicate that the recalibration will reduce these differences even further.

In stable conditions with no fog present, TC 3.0 does a fair job of parameterizing all of the transfer coefficients, but with a slightly larger difference with direct estimates. In stable conditions we can see a slight overestimation of both the Dalton number and the Stanton number as in the bottom panels of figures 4.1 and 4.3. From the bottom panel of figure 4.5, we see that TC 3.0 shows good agreement for C_K in stable conditions.
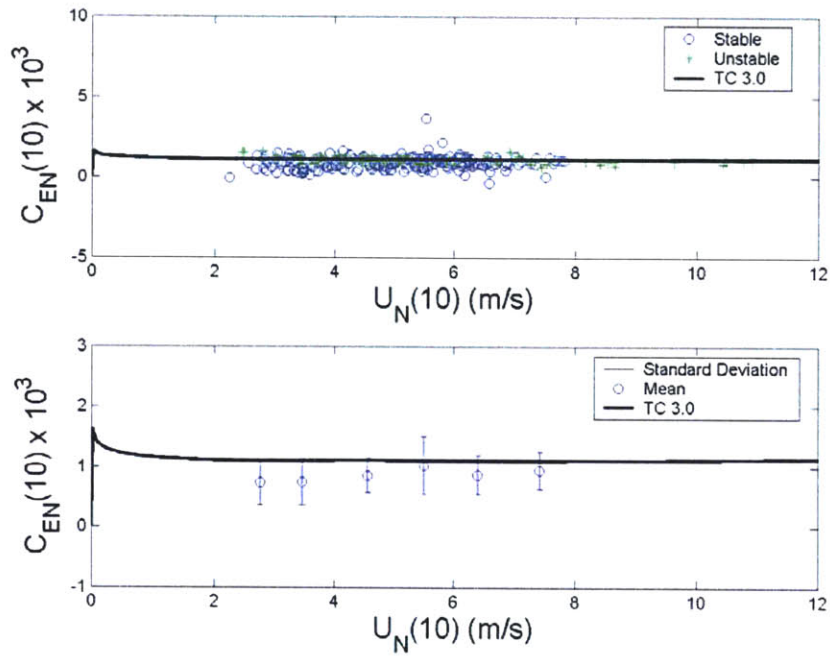
Figure 4.1 Neutral Dalton Number

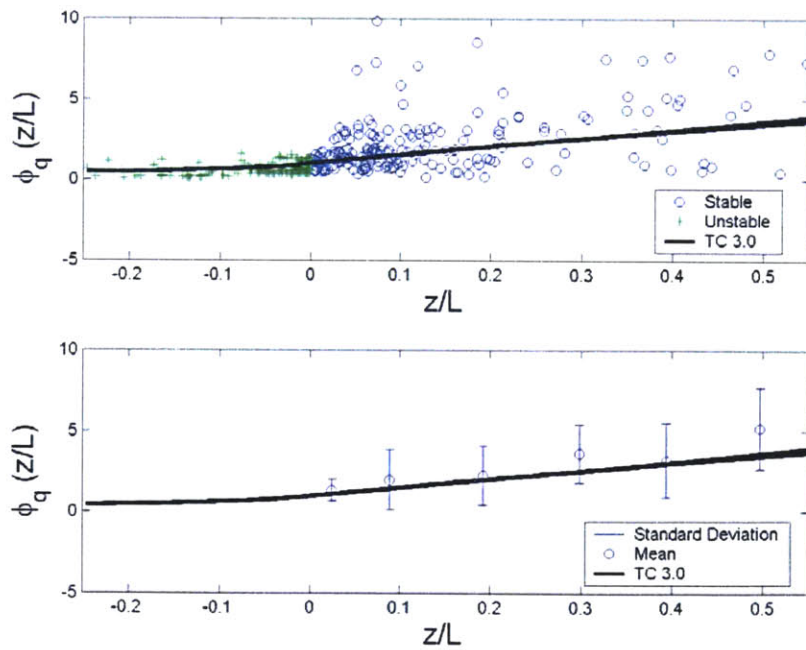Figure 4.2 Dimensionless Moisture Flux

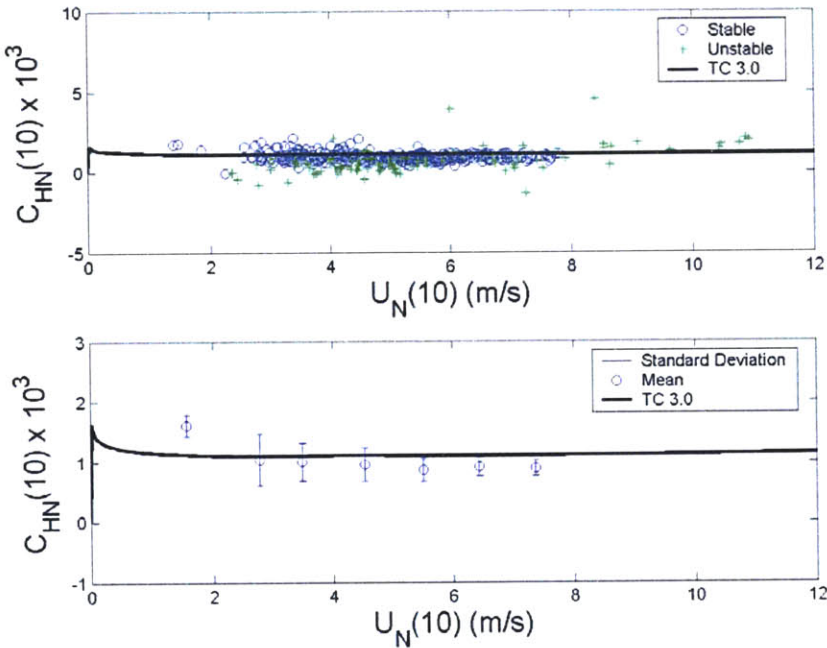Figure 4.3 Neutral Stanton Number
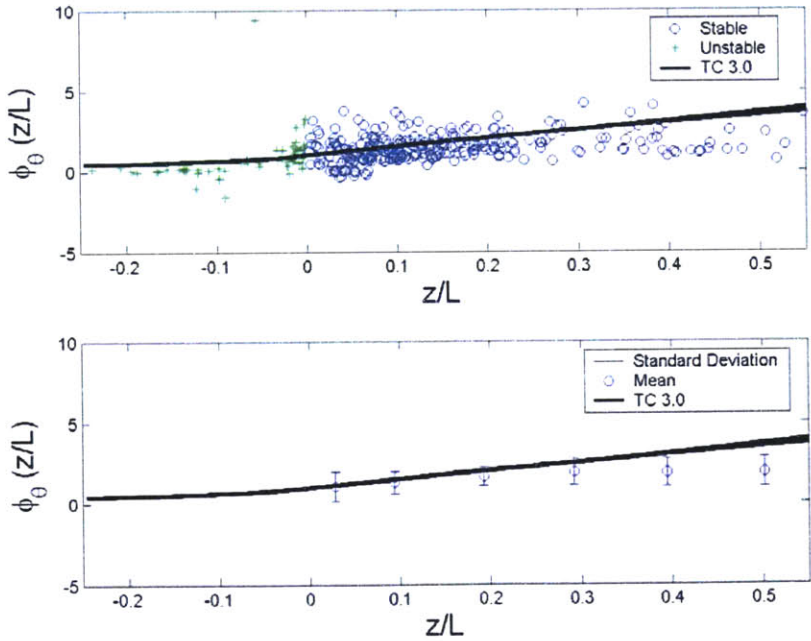

Figure 4.4 Dimensionless Heat Flux

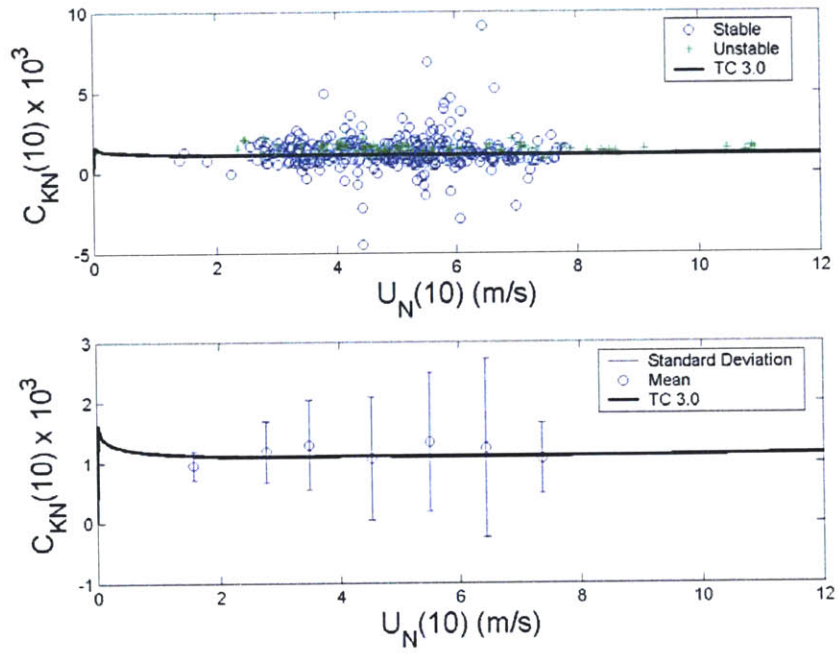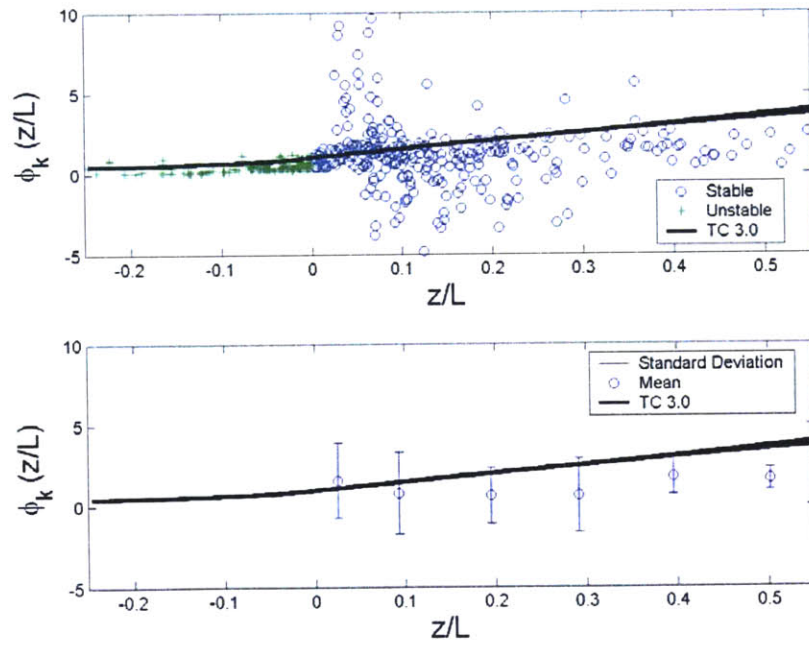Figure 4.5 Neutral Enthalpy Coefficient

Figure 4.6 Dimensionless Enthalpy Flux

Although upon closer examination one could argue that TC 3.0 slightly overestimates C_K.

A possible source of error in the TC 3.0 parameterizations of C_E, C_H, and C_K could be due to the improper parameterization of ϕ_q, ϕ_θ, and ϕ_k in stable conditions. By examining the behavior of the TC 3.0 dimensionless flux parameterizations in stable conditions we can clearly see that it is not quite as good as the parameterizations in unstable conditions. In figure 4.2, TC 3.0 consistently underestimates ϕ_q but not to a great degree. In figure 4.4, TC 3.0 does fairly well with ϕ_θ in near neutral to low stability but appears to degrade by increasingly overestimating as stability increases. In figure 4.6, TC 3.0 consistently overestimates ϕ_k in stable conditions. Since enthalpy is a combination of LHF and SHF, one would generally expect a direct correlation between the errors in the ϕ_q and ϕ_θ parameterizations and the error in the ϕ_k parameterization. Based on the results in figures 4.2, 4.4 and 4.6, it appears that ϕ_θ has a greater effect on ϕ_k than does ϕ_q in stable conditions with fog. This implies that the sensible heat flux dominates the enthalpy exchange when the flow is highly stratified in this data set. Nonetheless, these results suggest that the presence of water vapor does indeed affect the enthalpy and therefore the net energy exchange between the ocean and the atmosphere. Even with the correction factors added to the equations for the enthalpy, the discrepancy still persists. It also appears quite possible that the deficiencies in the TC 3.0 parameterizations for ϕ_q, ϕ_θ, and ϕ_k might be possible sources for the deficiencies in the TC 3.0 parameterizations for C_E, C_H, and C_K. This relation is illustrated in equations (3.1.9), (3.2.9), (3.2.15), (3.2.14) and (3.2.13). However, other possible sources of error may indeed be present.

4.3 Liquid Water Corrections and Fog

The instruments used to measure $\overline{w'q'}$ were the LI-7500 open path hygrometers listed in table 2.1. According to a design engineer, "the measurement principle and the measurement electronics of the LI-7500 should focus on the gaseous phase of water vapor. Water droplets in the LI-7500 measurement path will scatter "some" light on an absorption phenomena but the net effect on the output from the H_2O channel when water vapor is super saturated should be minimal, but it is not zero. What that small non-zero value is, is difficult to quantify." (Anderson 2004). As a result, the LI-7500 in correlation with the sonic anemometers gives the water vapor mass flux $\overline{w'\rho_v'}$ with a small amount of error due to the presence of the water droplets. Unfortunately, neither liquid water nor the liquid water flux were measured during the experiment. Therefore, for the purposes of calculations, we further assumed that $\overline{w'q_w'} \ll \overline{w'q'}$, and ignored the liquid water flux in equations (3.4.34) and (3.4.35). To estimate the liquid water content, we used the results given by Wallace and Hobbs (1977), as shown in figure 4.7. Wallace and Hobbs (1977) report values of $\overline{\rho}_w$ between 0.05 and 0.1 $\frac{g}{m^3}$ in fog, which is equivalent to $\overline{q}_w$ between 0.04 and 0.8 $\frac{g}{kg}$. The larger value was then incorporated into equations (3.4.34) and (3.4.35) with our assumption of zero liquid water flux for foggy conditions.

Figures 4.7 through 4.12 are the same plots as figures 4.1 through 4.6 with the data from foggy conditions calculated using equations (3.4.34) and (3.4.35) plotted over them. With respect to the previous discussion of the results shown in figures 4.1 through 4.6, the results of the additional consideration of water droplets in the equations show a very slight improvement in C_H, but a slight degradation in C_E and C_K when compared with the fog-free conditions. Although the inclusion of q_w slightly reduces the discrepancy between fog and fog-free conditions, we see that in fog TC 3.0 underestimates ϕ_q more than it did in stable conditions without fog. Likewise, in figure

60

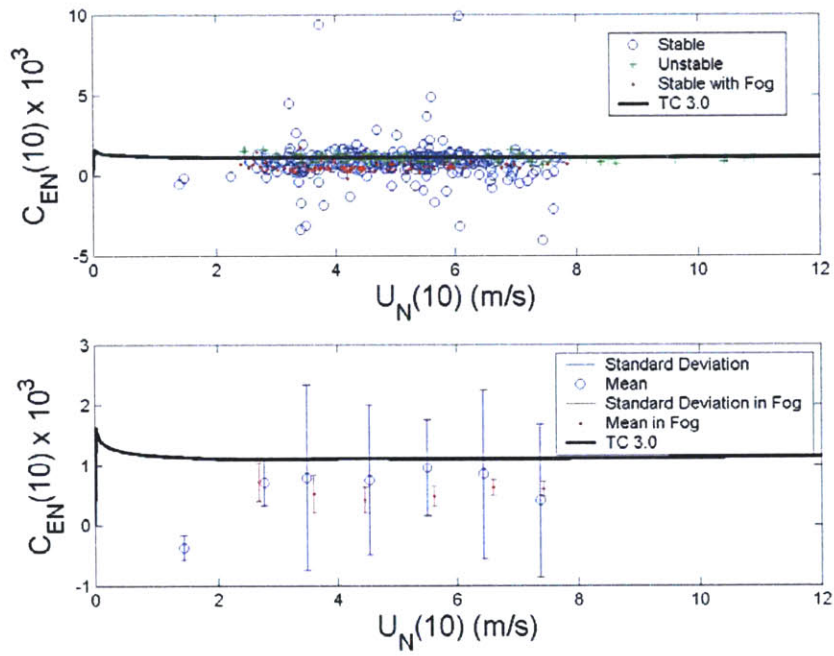Figure 4.7 Neutral Dalton Number with Liquid Water

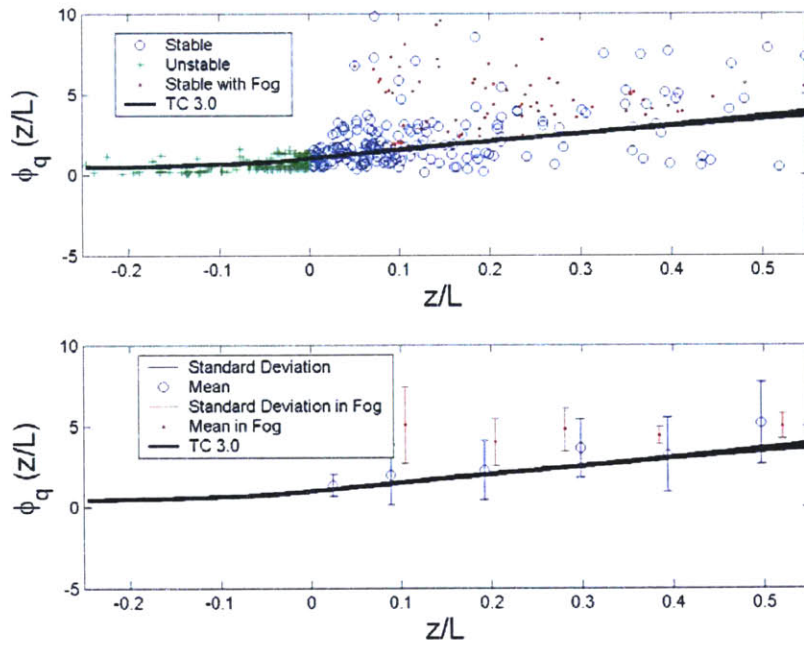Figure 4.8 Dimensionless Moisture Flux with Liquid Water

Figure 4.9 Neutral Stanton Number with Liquid Water
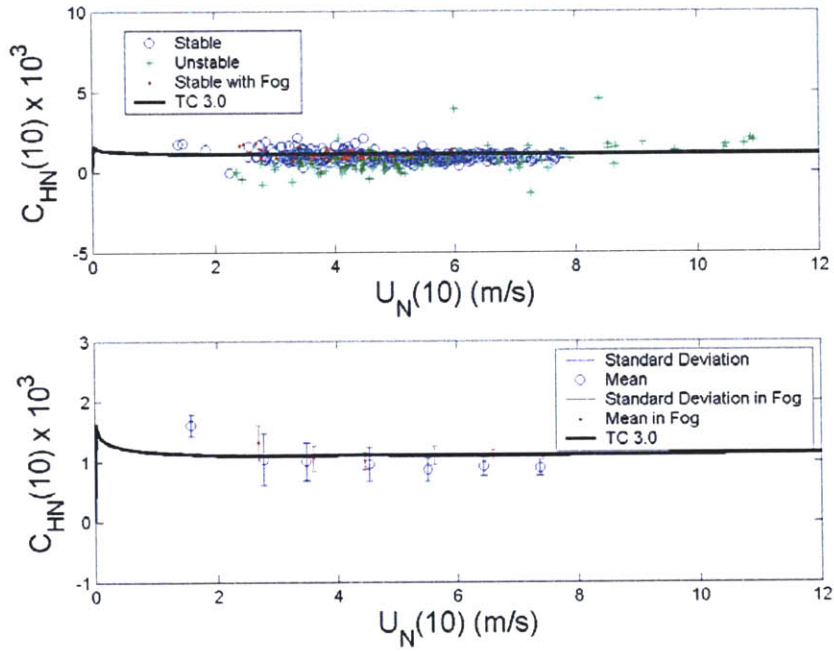
Figure 4.10 Dimensionless Heat Flux with Liquid Water
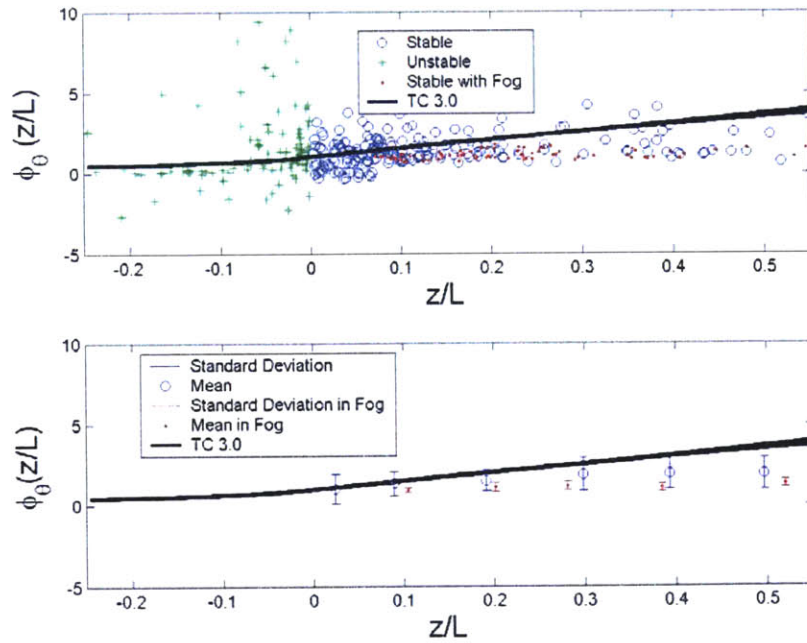
Figure 4.11 Neutral Enthalpy Coefficient with Liquid Water
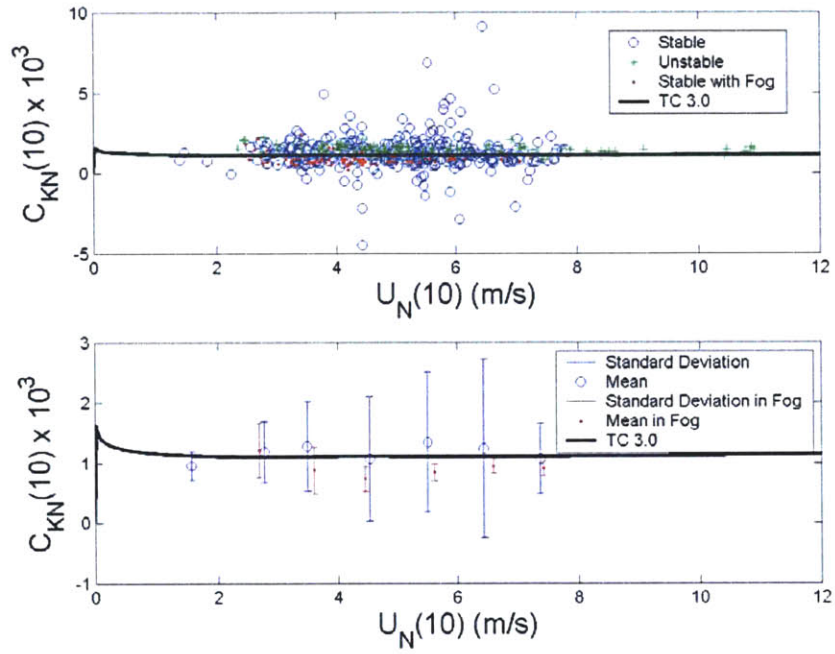
Figure 4.12 Dimensionless Enthalpy Flux with Liquid Water
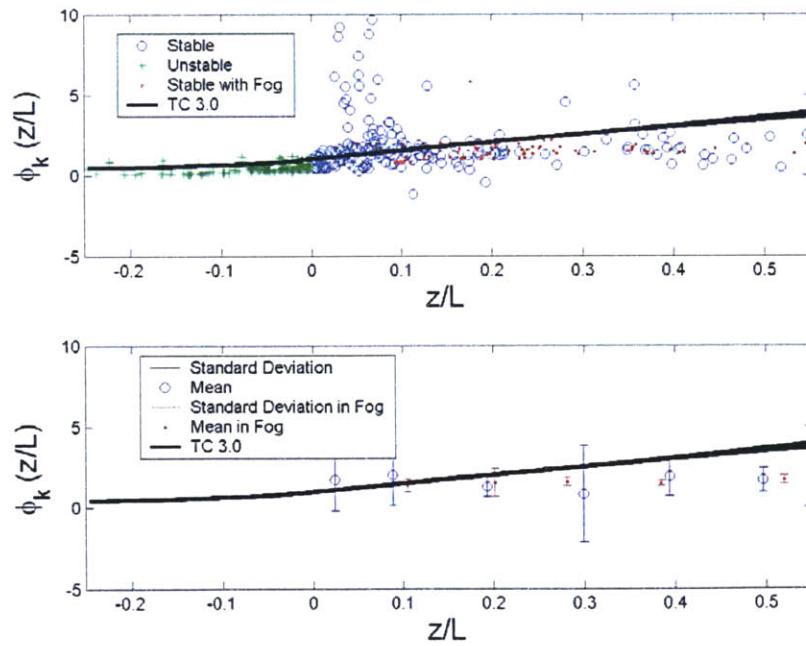
Figure 4.13 Fog Droplet Concentration Taken from Wallace and Hobbs, 1977
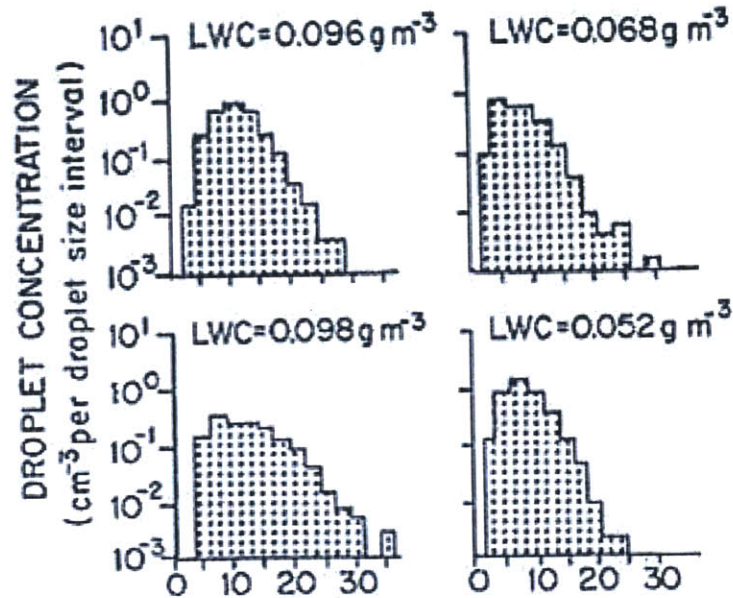
4.10, TC 3.0 overestimates ϕ_θ more than it did in stable conditions without fog. In figure 4.12, these differences appear to cancel each other in the calculation of ϕ_k as there is very little change from stable conditions without fog. These results indicate that the inclusion of q_w cannot explain the apparent differences. Further investigations are hampered by the lack of liquid water fluxes.

.

5. CONCLUSIONS

5.1 Discussion

The goal of this thesis was either to prove the incapability of the MOS based TC 3.0 parameterizations in their present form to account for the proper representation of the scalar fluxes, and to identify other possible mechanisms that may be causing observed differences between the data and parameterization. The results presented in thesis present strong evidence that MOS based TC 3.0 parameterizations for scalar fluxes, the moisture flux in particular, are indeed insufficient in stable conditions with fog.

This case study, which was a subset of the CBLAST experiment, shows that systematic differences between the observations and parameterization persist throughout all the corrections applied during the course of the analysis. One possible source of error for this deficiency is instrument error. As mentioned in section 4.2.3, the LI-7500 hygrometer is not expected to measure the liquid water flux. However, the effects of liquid water on the instrument reading are relatively unknown. To identify and quantify this error will require more specialized measurements or techniques. Additionally, it is not entirely certain that there was no trace of condensation on the infrared windows of the hygrometers when fog was present. Future work will incorporate the internal instrument diagnostic logged during the experiment. The use of these diagnostics will help to remove data when condensation is a problem.

Our analysis has shown that the distinct difference between TC 3.0 and the observation persists in stable conditions even when the foggy cases are removed. Therefore, a more intriguing explanation of this discrepancy is the possibility that there are still microscale physical processes present in fog that we still have yet to discover. Recall that we have measured all the terms in the 1-D scalar variance budget. This investigation will therefore continue by using this budget to determine, e.g., the relative importance of the individual terms and how they compare with previous field studies (Edson and Fairall 1998). If the most important processes in fog formation and

development occur below one meter, perhaps more measurements closer to the sea surface will provide further insights. This, of course, becomes quite challenging due to swell and wave action.

5.2 Future Work

The results of this case study have shown that there is much work yet to be done towards understanding the complex physical processes taking place in stable conditions with fog. The ultimate goal of future work in this field is the improvement of the TC 3.0 parameterizations under these conditions. One of the first steps to be taken toward this goal would be a closer look at how the instruments were calibrated. As any field scientist knows, an essential factor in any field experiment is proper instrument calibration. If the instruments used to measure the moisture fluxes during this experiment were not properly calibrated, this would certainly introduce errors. More precise calibration techniques will be applied to the data collected during this case study and throughout all of the data collected during CBLAST, in combination with consideration of the above mentioned diagnostics.

As mentioned in section 3.4, improper parameterization of ϕ_q and therefore ψ_q could be possible sources of error in the parameterization of C_E in stable conditions. Therefore, a modification of the ϕ_q and ψ_q parameterizations will be investigated. Additionally, could the assumption of $\overline{w'q_w'} \approx 0$ be incorrect? The results from section 4.3 suggest yes. If the LI-7500 is only measuring $\overline{w'q'}$, the inclusion of $\overline{w'q_w'}$ would increase the downward flux of total water and , perhaps, improve the comparison.

In section 3.2, the roughness length, z_q, was introduced, yet no analysis of its effect on the parameterization of C_E or ϕ_q was investigated in this case study. In light of the amount of work yet to be done to improve the overall quality of the analysis, we felt this was premature. However, once this work is completed, future studies will

incorporate how estimates of z_q compare with TC 3.0 using improved estimates of ϕ_q and ψ_q.

The proper parameterizations of the LHF and SHF by models such as COAMPS are very important, especially in a stable boundary layer. These flux parameterizations, in addition to the surface stress parameterization, directly impact moisture, temperature and wind speed, near the surface. This in turn affects the higher level boundary layer structure including fog, clouds, and the low-level jet. In addition, fog development is very sensitive to SST which cools down and dries the low-level air under stable and saturation surface conditions. Since the stable surface layer is usually shallow, the errors in the LHF parameterization will greatly impact the saturation condition in the low levels. From figure 1.1, it can be seen that TC 3.0 overestimates LHF by as much as $10 \frac{W}{m^2}$ in stable conditions with fog. While the cumulative effect on the heat balance may be large, it is unclear how much of an effect a $10 \frac{W}{m^2}$ error in the LHF would have on the SST over shorter time scales. Fog will also likely be sensitive to the stress which generates turbulent mixing thereby effecting fog development (Wang 2004).

In conclusion, further studies need to be conducted under stable conditions with fog to gain sufficient insight to develop improved parameterizations of scalar fluxes. Ideally, these investigations should be a combination of observational and modeling studies. Such an investigation has recently begun between WHOI and NRL Monterey. If an improved version of the TC 3.0 parameterization of the sensible and latent heat fluxes become utilized in COAMPS, there should be a significant improvement in the forecasting ability of the model. In turn, this will improve the Navy's ability for safe navigation and more accurate and effective mission planning.

APPENDIX A

The discussion of the expansion of equation (3.4.14) from Edson (2004) is given by Businger (1982) and depends on the constraint of zero vertical mass flux for dry air:

$$\overline{\rho_a w} = 0$$

He uses this accepted governing constraint to derive an expression for the total mass flux (assuming no liquid water):

$$\overline{\rho w} = \overline{\rho_a w} + \overline{\rho_v w} = \overline{\rho(1-q)w} + \overline{\rho_v w} = \overline{\rho_v w} \approx \overline{\rho w' q'}$$

However, the equally careful investigation by Webb et al. (1980) gives:

$$\overline{\rho w} = \frac{\overline{\rho w' q'}}{(1-\overline{q})}$$

Using this form of the total mass flux gives the following expansion:

$$\overline{(1-q)\rho c_{pd} T} = \overline{\rho w' T'} c_{pd} (1-q)$$

$$\overline{\rho w q L_e} = \overline{\rho q} \left(c_{pv} - c_{pw} \right) \overline{w' T'} + \overline{\rho} L \frac{\overline{w' q'}}{(1-\overline{q})}$$

$$\overline{\rho w q c_{pw} T} = \overline{\rho q} c_{pw} \overline{w' T'} + c_{pw} \overline{\rho} \overline{T} \frac{\overline{w' q'}}{(1-\overline{q})}$$

$$\overline{\rho w b_{m2}} = \overline{\rho} \frac{\overline{w' q'}}{(1-\overline{q})}$$

APPENDIX B

This expansion of equation (3.4.32) from Edson (2004) begins by considering the mass flux. With liquid water included, the mass flux becomes:

$$\overline{\rho w} = \overline{\rho_a w} + \overline{\rho_v w} + \overline{\rho_w w} = \overline{\rho(1-q-q_w)w} + \overline{\rho q w} + \overline{\rho q_w w}$$

As in Businger (1982), no contribution from horizontal convection is considered:

$$\overline{\rho_a w} = \overline{\rho(1-q-q_w)w} = 0$$

$$\overline{\rho w} = \overline{\rho_v w} + \overline{\rho_w w} = \frac{\overline{\rho}}{(1-\overline{q}-\overline{q_w})}\left(\overline{w'q'} + \overline{w'q'_w}\right) = \overline{\rho_a}\,\overline{w'r'} + \overline{\rho_a}\,\overline{w'r'_w}$$

The expansion of terms in (3.4.32) now become:

$$\overline{\rho w(1-q-q_w)c_{pd}T} = \overline{\rho}c_{pd}\overline{w'T'}(1-\overline{q}-\overline{q_w})$$

$$\overline{\rho w(q+q_w)c_{pw}T} = \overline{\rho}c_{pw}(\overline{q}+\overline{q_w})\overline{w'T'} + \overline{\rho}c_{pw}\frac{1}{(1-\overline{q}-\overline{q_w})}\left(\overline{w'q'} + \overline{w'q'_w}\right)$$

$$\overline{\rho w q L_e} = \overline{\rho}\overline{q}\left(c_{pv} - c_{pw}\right)\overline{w'T'} + \overline{\rho}\overline{L_e}\frac{1}{(1-q-q_w)}\left(\overline{w'q'} + \overline{w'q'_w}\right)$$

$$\overline{\rho w b_{m3}} = \overline{\rho}\frac{1}{(1-q-q_w)}\left(\overline{w'q'} + \overline{w'q'_w}\right)b_w$$

BIBLIOGRAPHY

Anderson, D. (2004). LI-7500 open path CO2/H2O gas analyzer. R. Crofoot. Woods
    Hole, MA.
Austin, T. C., J. B. Edson, et al. (2002). "A Network Based Telemetry Architecture
    Developed for the Martha's Vineyard Coastal Observatory." IEEE Journal of
    Oceanic Engineering 27(2): 228-234.
Binhua, W. (1985). Sea Fog. New York, Springer-Verlag.
Bradley, E. F., P. A. Coppin, et al. (1991). "Measurements of Sensible and Latent Heat
    Flux in the Western Equatorial Pacific Ocean." Journal of Geophysical Research
    96(Supplement): 3375-3389.
Businger, J. A. (1982). "The Fluxes of Specific Enthalpy, Sensible Heat and Latent Heat
    near the Earth's Surface." Journal of the Atmospheric Sciences 39(8): 1889-1894.
Champagne, F. H., C. A. Friehe, et al. (1977). "Flux measurements, flux estimation
    techniques, and finescale turbulence measurements in the unstable surface layer
    over land." Journal of the Atmospheric Sciences 34: 515-530.
Edson, J. B. (2003). Inclusion of Gustiness. Woods Hole, MA.
Edson, J. B. (2004). Flux Profile Relationships in the Marine Atmospheric Surface Layer
    During CBLAST. Ocean Sciences Meeting, Portland, OR.
Edson, J. B. and C. W. Fairall (1998). "Similarity Relationships in the Marine
    Atmospheric Surface Layer for Terms in the TKE and Scalar Variance Budgets."
    Journal of the Atmospheric Sciences 55: 2311-2328.
Edson, J. B. and W. McGillis (2003). Air-Side Measurements of Momentum, Heat and
    Mass Exchange During CBLAST-Low. Woods Hole, MA.
Edson, J. B., W. R. McGillis, et al. (2003). The Coupled Boundary Layers and Air-Sea
    Transfer Experiment in Low to Moderate Winds (CBLAST-Low). Woods Hole,
    MA, Woods Hole Oceanographic Institution: 12.
Edson, J. B., C. J. Zappa, et al. (2002). Scalar Flux Profile Relationships over the Open
    Ocean. Woods Hole, MA, Woods Hole Oceanographic Institution: 26.
Edson, J. B., C. J. Zappa, et al. (2004). "Scalar flux profile relationships over the open
    ocean." Journal of Geophysical Research in revision.
Fairall, C. W., E. F. Bradley, et al. (2003). "Bulk Parameterization of air-sea fluxes:
    Updates and verification for the COARE algorithm." Journal of Climate and
    Applied Meteorology 16: 571-591.
Fairall, C. W., E. F. Bradley, et al. (1996). "Bulk Parameterization of air-sea fluxes for
    Tropical Ocean-Global Atmosphere Coupled-Ocean Atmosphere Response
    Experiment." Journal of Geophysical Research 101(C2): 3747-3764.
Farrar, T. (2004). Observations of Coupled Air-Sea Boundary Layers During CBLAST.
    Ocean Sciences Meeting, Portland, OR.
Frank, W. M. and G. D. Emmitt (1981). "Computation of vertical total energy fluxes in a
    moist atmosphere." Boundary-Layer Meteorology 21: 223-230.
Frew, N. (2004). Surface Film Distributions During CBLAST. Ocean Sciences Meeting,
    Portland, OR.

Gerber, H. E. (1981). "Microstructure of a Radiation Fog." Journal of the Atmospheric Sciences **38**: 454-458.

Grachev, A. A., C. W. Fairall, et al. (2003). "Wind Stress Vector over Ocean Waves." Journal of Physical Oceanography **33**: 2408-2429.

Hara, T., E. J. Bock, et al. (1998). "Observations of short wind waves in coastal waters." Journal of Physical Oceanography **28**: 1425-1438.

Hare, J. E., P. O. G. Persson, et al. (1999). Behavior of Charnock's realtionship for high wind conditions. 13th Symposium on Boundary Layers and Turbulence, Dallas, TX, American Meteorological Society.

Hintsa, E. J., J. W. H. Dacey, et al. (2004). "Sea-to-air fluxes from measurements of the atmospheric gradient of dimethylsulfide and comparison with simultaneous relaxed eddy accumulation measurements." Journal of Geophysical Research **109**.

Hristov, T. (2004). Atmospheric Pressure Fluctuations over the Open Ocean. Ocean Sciences Meeting, Portland, OR.

Izumi, Y. (1971). Kansas 1968 field program data report. Hanscom AFB, MA, Air Force Cambridge Research Lab: 79.

Janssen, P. A. E. M. (1999). "On the Effect of Ocean Waves on the Kinetic Energy Balance and Consequences for the Inertial Dissipation Technique." Journal of Physical Oceanography **29**(3): 530-534.

Large, W. G. and S. Pond (1982). "Sensible and Latent Heat Flux Measurements over the Ocean." Journal of Physical Oceanography **12**(5): 464-482.

Louis, J.-F. (1979). "A Parametric Model of Vertical Eddy Fluxes in the Atmosphere." Boundary-Layer Meteorology **17**: 187-202.

Lundquist, J. (2000). California and Oregon Coastal Humidity and Fog. Oceanography. San Diego, CA, University of California, San Diego: 139.

Mahrt, L. (2004). The Very Stable Marine Boundary Layer. Ocean Sciences Meeting, Portland, OR.

Mahrt, L., D. Vickers, et al. (1996). "Sea surface drag coefficients in RASEX." Journal of Geophysical Research **101**: 14327-14335.

McWilliams, J. (2004). Surface Wave Effects in the Oceanic Boundary Layer. Ocean Sciences Meeting, Portland, OR.

Monin, A. S. and A. M. Obukhov (1954). "Basic laws of turbulent mixing in the surface layer of the atmosphere." Trudy Geofiz. Inst. **Aca. Nauk SSSR**(24): 163-187.

Paulson, C. A. (1970). "Mathematical representation of wind speed and temperature profiles in the unstable atmospheric boundary layer." Journal of Applied Meteorology **9**: 857-861.

Persson, O. G. P., C. W. Fairall, et al. (2002). "Measurements near the Atmospheric Surface Flux Group tower at SHEBA: Near-surface conditions and surface energy budget." Journal of Geophysical Research **107**(C10): 8045.

Poulos, G. S., W. Blumen, et al. (2002). "CASES-99: A comprehensive investigation of the stable nocturnal boudary layer." Bulletin of the American Meteorological Society **83**: 555-581.

Sabersky, R. H., E. G. Hauptmann, et al. (1998). Fluid Flow: A First Course in Fluid Mechanics. Upper Saddle River, NJ, Pearson Education.

Smith, S. D. (1988). "Coefficients for sea surface wind stress, heat flux, and wind profiles as a function of wind speed and temperature." Journal of Geophysical Research **93**: 15467-15472.

Stull, R. B. (1988). An Introduction to Boundary Layer Meteorology. Boston, Kluwer Academic Publishers.

Sullivan, P. (2004). Large Eddy Simulations of Low Wind Boundary Layers in the Presence of Waves. Ocean Sciences Meeting, Portland, OR.

Turton, J. D. and R. Brown (1987). "A comparison of a numerical model of radiation fog with detailed observations." Quarterly Journal of the Royal Meteorological Society **113**: 37-54.

Vickers, D. (2004). Shallow Marine Boundary Layers. Ocean Sciences Meeting, Portland, OR.

Wallace, J. W. and P. V. Hobbs (1977). Atmospheric Science: An Introductory Survey. San Diego, CA, Academic Press, Inc.

Wang, S. (2004). Moisture Physics and Flux Parameterizations in COAMPS. R. Crofoot. Cambridge, MA.

Webb, E. K., G. I. Pearman, et al. (1980). "Correction of flux measurements for density effects due to heat and water vapor transport." Quarterly Journal of the Royal Meteorological Society **106**: 85-100.

Welch, R. M., M. G. Ravichandran, et al. (1986). "Prediction of Quasi-Periodic Oscillations in Radiation Fogs. Part I: Comparison of Simple Similarity Approaches." Journal of the Atmospheric Sciences **43**(7): 633-651.

Welch, R. M. and B. A. Wielicki (1986). "The Stratocumulus Nature of Fog." Journal of Climate and Applied Meteorology **25**(2): 101-111.

Weller, B. (2004). Spatial and Temporal Scales of Oceanic Variability in CBLAST Region. Ocean Sciences Meeting, Portland, OR.

Wyngaard, J. C., N. E. Busch, et al. (1973). Workshop on Micrometeorology. Boston, MA, American Meteorological Society.